Univerzita Pavla Jozefa Šafárika v Košiciach
Prírodovedecká fakulta

Magnetismus ve sloučeninách $REFe_2Si_2$, RE = vzácnozeminný kov

Diplomová práca

Košice 2004

Matúš Mihalik

Abstract

In this diploma work, the magnetic properties, heat capacity and electrical resistivity of RFe_2Si_2 intermetallic compounds (R = Pr, Tb and Gd) have been studied on single crystals grown by Czochralski method. All compounds undergo an antiferromagnetic phase transition at temperatures 7.2 K, 5.2 K and 8 K, respectively and a field induced magnetic transition into the ferromagnetic state in field less than 1 T. The magnetization and susceptibility measurements revealed strong uniaxial anisotropy with $c-$axis as an easy axis on $PrFe_2Si_2$ and $TbFe_2Si_2$. Small anisotropy was detected in $GdFe_2Si_2$ case. Due to the strong anisotropy even in paramagnetic state the susceptibility of $PrFe_2Si_2$ and $TbFe_2Si_2$ does not follow the Curie–Weiss law, but in the case of $GdFe_2Si_2$ the Curie–Weiss law is valid. Using comparative analysis of specific heat we separated magnetic contribution to the specific heat and determined the ground-level splitting caused by the crystal electric field. Resistivity measurements in paramagnetic region revealed small deviations from Bloch-Grüneissen law and strong anisotropic behavior. In magnetoresistivity measurements we observed dependency like field-induced ferromagnetic state.

This work is part of the research program MSM113200002 that is financed by the Ministry of Education of the Czech Republic. Part of this work was also supported by the Grant Agency of the Czech Republic (Grant No. 106/02/0940) and VEGA of the Slovak Republic No. 2/4050/04.

Anotácia

Táto diplomová práca sa zaoberá magnetickými vlastnosťami, merným teplom a elektrickým odporom monokryštálov intermetalických zlúčenín typu RFe_2Si_2 kde (R = Pr, Tb and Gd) získaných pomocou Czochralského metódy. $PrFe_2Si_2$, $TbFe_2Si_2$ a $GdFe_2Si_2$ sa usporiadavajú antiferomagneticky pri teplotách 7.2 K, 5.2 K a 8 K. Vo všetkých zlúčeninách bol pozorovaný poľom indukovaný prechod do feromagnetického stavu pri poliach nižších ako 1 T. Merania magnetizácie a susceptibility na $PrFe_2Si_2$ a $TbFe_2Si_2$ odhalili silnú magnetokryštalovú anizotropiu s $c-$osou ako ľahkou osou magnetizácie. Magnetizačné merania na $GdFe_2Si_2$ neodhalili magnetokryštalovú anizotropiu a teplotná závislosť susceptibility vyhovuje Curie-Weissovmu zákonu. S využitím porovnávacej analýzy merného tepla sme odseparovali magnetický príspevok k mernému teplu a určili rozštiepenie základného stavu sdpôsobené kryštálovým poľom. Odporové merania odhalili silné anizotropné chovanie a odchylky od Bloch-Grünheissenovho zákona. Anomália spojená s teplotou usporiadania bola pozorovaná pri $TbFe_2Si_2$ a $GdFe_2Si_2$. V meraniach magnetorezistencie sme pozorovali závislosti podobné indukovanému feromagnetickému stavu.

Táto práca je časť výskumného programu MSM113200002, ktorý je financovaný Ministerstvom Školstva Českej republiky a časť práce bola tiež podporená Grantovou agentúrou Českej republiky (Grant č. 106/02/0940) a VEGA Slovenskej republiky č. 2/4050/04.

Acknowledgement

First of all I would like to thank to the God. He was the only one who didn't desert me in all my hard times, when I wrote this diploma work. And he didn't desert me even in all my very nice moments, too.

At the second place I would like to thank to Prof. RNDr. Vladimír Sechovský, DrSc. who encountered me to his experimental group. He decided to be the supervisor of my diploma work and allowed me to use experimental apparatus in order to obtain all experimental results presented in this diploma work.

Next, I would like to express my thanks to Ing. Josef Šebek PhD., Ing. Eva Šantavá, CSc. and Mgr. Jana Vejpravová who helped me to understand experimental apparatus PPMS from Quantum Design and who gave me suggestions about strategy of experimental measurements.

For help with X-ray powder diffraction and analyzing data from powder diffraction spectra I would like to thank to Dr. Stanislav Daniš.

Doc. RNDr. Martin Diviš, CSc. helped me with theoretical concepts of my diploma work. He explained me some measured effects from theoretical point of view and I would like to address my thanks to him, too.

I offer my thanks to doc. RNDr. Pavel Svoboda, CSc. who helped me with sample preparation, explained me crystal growth by Czochralski method in a tri-arc furnace. Together with Prof. RNDr. Vladimír Sechovský, DrSc. and Mgr. Jana Vejpravová in many fruitful discussion he gave me important suggestions concerning interpretation of the obtained experimental results.

Doc. RNDr. Pavol Sovák, CSc. and management of Faculty of Science, P. J. Šafárik University, allowed me to make individual study program and enable my stay at Charles University, Prague, for four semesters to work on my diploma work there. I am thankful them for all assistance and understanding, which they provided me.

At the end, I express my thanks to my parents who brought me up to the person I am now. They always offered me hinterland in all aspects I needed.

Prehlasujem, že som diplomovú prácu vypracoval samostatne, za pomoci odbornej literatúry, ktorú uvádzam v zozname

Košice, apríl 2004

Matúš Mihalik

Contents

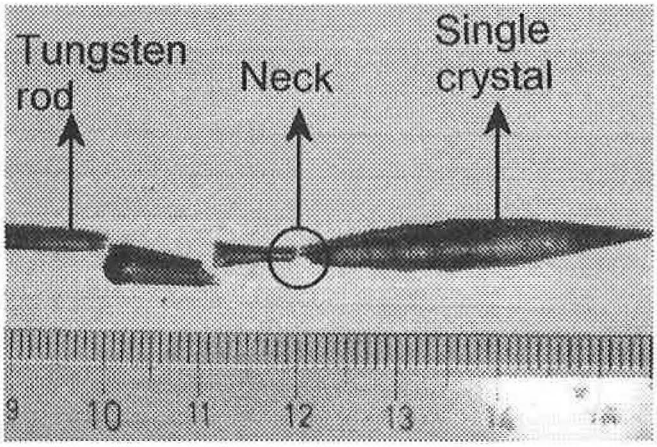

Figure 2.6: Single crystal of $DyFe_2Si_2$ grown by Czochralski method.

Compound	a (Å)	c (Å)	z (relative)	RRR $a-$axis	RRR $c-$axis
$PrFe_2Si_2$	4.0037	10.0542	0.3700	6.9	7.5
$TbFe_2Si_2$	3.9195	9.9594	0.3737	5.1	6.8
$GdFe_2Si_2$	3.9400	9.9939	0.3745	7.3	5.9

Table 2.2: The refined crystallographic parameters and RRR (can be understand as quality index of the crystal) for the studied $REFe_2Si_2$ compounds.

phase with the saturated magnetization about 2 μ_B/f.u. we can estimate the amount of this impurity as less then 0.2 %.

The easy-growth axis of the crystal is in basal plane. The resulting crystals are very brittle and in all cases the plane perpendicular to the $c-$axis is an easy cleaving plane. Because of this, it was very difficult to prepare samples for measurement along the $c-$axis. Along the $c-$axis the error in electric transport measurements is almost 4 times higher than along the $a-$axis.

2.3.2 Magnetic properties.

$PrFe_2Si_2$

Magnetization measurements of $PrFe_2Si_2$ revealed strong uniaxial anisotropy. The easy axis of magnetization is the $c-$axis (see fig. 2.8). The signal along $a-$axis is weak and linear up to field 9 T. The measurements along $c-$axis shows hysteresis up to the field $B = 14$ T. The hysteresis can be observable even in paramagnetic region. The magnetic moment in 14 T is $\mu = 2.25\mu_B$/f.u. which is less than magnetic moment of Pr^{3+} ion (3.5 μ_B).

Chapter 1

Theory

1.1 Magnetism

1.1.1 Hund's rules

In free atom, one-electron levels are characterized by orbital angular momentum l. For given l there are $2l + 1$ values of l_z and two possible spin orientations, so on shell with orbital number l can be $n \leq 2(2l + 1)$ electrons. For non interacting electrons the ground state is degenerate, which reflects the large number of ways to put n electrons into shell. However, this degeneracy is lifted by electron–electron Coulomb interaction as well as by the electron spin–orbit interaction. If we exclude the heaviest ions and in the case that the degeneracy is already lifted, the lowest–lying levels can be described by a simple set of rules:

1. **Russel–Saunders Coupling**: According to this rule, the total angular momentum is a sum of electronic total spin and orbital angular momentum $\mathbf{J} = \mathbf{L} + \mathbf{S}$. There are several exceptions from this rule, for example "quenching" of the orbital angular momentum caused by crystal field splitting.

2. **Hund's First Rule**: The system of n electrons have the lowest energy, when spins of all electrons are in the same direction. So in a shell with $n \leq 2l+1$ all electrons will have a spin with the same orientation. Each next electron in this shell will have the opposite spin according to exclusion principle.

3. **Hund's Second Rule**: The total orbital angular momentum L of the lowest–lying states has the largest value that is consistent with Hund's first rule and with the exclusion principle. Thus the first electron in the shell will have $|l_z|$ equal to l, second will have $|l_z|$ equal to $(l - 1)$ etc.

4. **Hund's Third Rule**: The first and second Hund's rule determine values of L and S. The third Hund's rule determine value od J. According to this rule, the value J assumed in the state of lowest energy is:

$$J = |L - S| \text{ for } n \leq (2l+1);$$

$$J = L + S \text{ for } n \geq (2l+1)$$

Because the crystal field can be introduced as a perturbation on the (2S +1)(2L + 1)–fold set of states and this perturbation acts in addition to the spin–orbit coupling, the Hund's third rule must be modified for atoms with partially filled d–shell.

1.1.2 Diamagnetism and paramagnetism

From thermodynamic theory the susceptibility is defined by:

$$\chi = \frac{\partial M}{\partial H} = -\frac{1}{V}\frac{\partial^2 F}{\partial H^2} = -\frac{N}{V}\frac{\partial^2 \Delta E}{\partial H^2} \tag{1.1}$$

where F is the magnetic Helmholtz free energy and ΔE can be obtained from perturbation theory second–order term. In [1] they found:

$$\Delta E_n = \mu_B \mathbf{H} \cdot \langle n| \mathbf{L} + g_0 \mathbf{S} |n\rangle + \sum_{n' \neq n} \frac{|\langle n| \mu_B \mathbf{H} \cdot (\mathbf{L} + g_0 \mathbf{S}) |n'\rangle|^2}{E_n - E_{n'}} \tag{1.2}$$

$$+\frac{e^2}{8mc^2} H^2 \langle n | \sum_i (x_i^2 + y_i^2) | n \rangle$$

Larmour diamagnetism

Let us consider that we have ion with all electronic shells filled. In this case according to Hund's rules the ion has zero spin and orbital angular momentum in ground state:

$$\mathbf{J}|0\rangle = \mathbf{S}|0\rangle = \mathbf{L}|0\rangle = 0 \tag{1.3}$$

then equation 1.2 is reduced only to the third term and if we consider spherical symmetry of the ion we can find for susceptibility [1]:

$$\chi = -\frac{e^2}{6mc^2}\frac{N}{V}\langle 0| \sum_i r_i^2 |0\rangle \tag{1.4}$$

The equation 1.4 is known as Larmour diamagnetic susceptibility. The term diamagnetism means that applied field induce moments in opposite direction to the applied field, so in inhomogeneous fields diamagnetic sample tend to get to place where the external field is in local minimum.

Van Vleck paramagnetism

In the case of atom with the shell where the number of electrons is by one electron less than in half filled shell, in the ground state J = 0. In this case we can find for susceptibility [1]:

$$\chi = -\frac{N}{V}\left[\frac{e^2}{4mc^2}\langle 0| \sum_i (x_i^2 + y_i^2) |0\rangle - 2\mu_B^2 \sum_n \frac{|\langle 0| (\mathbf{L}_z + g_0 \mathbf{S}_z) |n\rangle|^2}{E_n - E_0}\right] \tag{1.5}$$

The first term of equation 1.5 is just the Larmour susceptibility mentioned above. The second term has opposite sign to Larmour susceptibility and is responsible for paramagnetic behavior. This paramagnetic term is known as Van Vleck paramagnetism. The magnetic ground state of atoms with the shell where the number of electrons is by one electron less than in half filled shell balances between two terms mentioned above.

Curie's law

For computing ground magnetic state of atom with $J \neq 0$ we can use the thermodynamics fundamental statistical rule:

$$e^{-F/(k_B T)} = \sum_n e^{-E_n(H)/(k_B T)} \tag{1.6}$$

If only $2J + 1$ states are thermally excited with appreciable probability (it means that there is no central field splitting and we neglect the higher excited states), then the free energy is given from equation 1.6 by:

$$e^{-\beta F} = \sum_{J_z=-J}^{J} e^{-\beta\gamma H J_z} \tag{1.7}$$

where $\gamma = g(JLS)\mu_B$ and $\beta = 1/(k_B T)$, where $g(JLS)$ is known as Landé $g-$factor and can be computed as:

$$g(JLS) = \frac{1}{2}(g_0 + 1) - \frac{1}{2}(g_0 - 1)\frac{L(L+1) - S(S+1)}{J(J+1)} \tag{1.8}$$

where g_0 is the electronic $g-$factor and its value is $g_0 = 2.0023$. Magnetization in thermodynamics can be defined as:

$$M = -\frac{N}{V}\frac{\partial F}{\partial H} \tag{1.9}$$

and then we will obtain for magnetization [1]:

$$M = \frac{N}{V}\gamma J B_J(\beta\gamma J H) \tag{1.10}$$

where $\mathrm{B}_J(\mathrm{x})$ is *Brillouin function*, which is defined by:

$$B_J(x) = \frac{2J+1}{2J}\coth\frac{2J+1}{2J}x - \frac{1}{2J}\coth\frac{1}{2J}x \tag{1.11}$$

Brillouin function $\mathrm{B}_J(x)$ for different J is plotted on figure 1.1. For small x (it means that $\gamma H \ll k_B T$) we can approximate hyperbolic cotangent by its Taylor queue up to $O(x^3)$ and than we can obtain for Brillouin function [1]:

$$B_J(x) \approx \frac{J+1}{3J}x + O\left(x^3\right) \tag{1.12}$$

Consequently we can obtain from definition 1.1 the Curie's law:

$$\chi = \frac{N}{3V}\frac{\mu_B^2 \mu_{eff}^2}{k_B T} \tag{1.13}$$

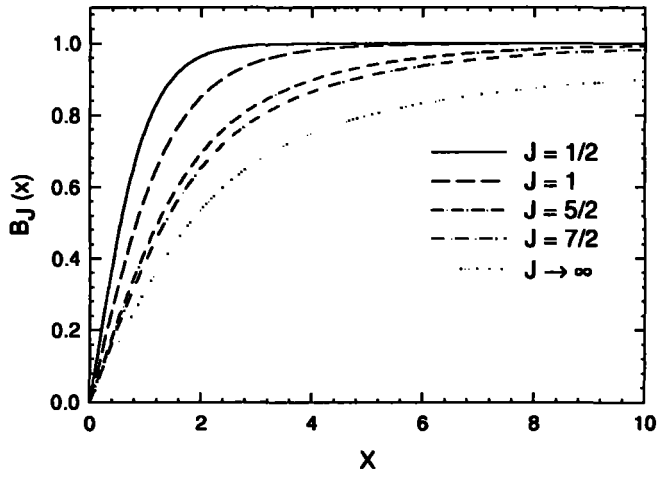

Figure 1.1: Theoretical dependency of Brillouin function for different total electronic angular momentum number J.

where μ_{eff} is effective moment defined as:

$$\mu_{eff} = g(JLS)\left[J\left(J+1\right)\right]^{1/2} \tag{1.14}$$

The Curie's law characterizes temperature dependence of paramagnetic systems with noninteracting permanent moments those alignment is favored by the field, and opposed by thermal disorder. In most cases the Curie's law is written as $\chi = C/T$ where C is constant temperature independent. It is important to note that this law is valid only under condition $k_B T \gg \gamma H$. For interacting moments Curie's law have to be modified by adding correction terms.

Curie–Weiss law

In compound, each spin feels the external field including the field from another spins, which can be described by the effective field $\mathbf{H}_{eff}$ [1]:

$$\mathbf{H}_{eff} = \mathbf{H} + \frac{1}{g\mu_B}\sum_{R'} J(\mathbf{R}-\mathbf{R}')\mathbf{S}(\mathbf{R}') \tag{1.15}$$

$\mathbf{H}_{eff}$ is an operator with complicate dependency on a detailed configuration of all other spins. According to Mean field approximation we can replace $\mathbf{H}_{eff}$ with its thermal equilibrium mean value and assume that each spin feels field $\mathbf{H}_{eff}$ (It means that the magnetization is function of $\mathbf{H}_{eff}$). This assumption we can accept only in the cases that each individual spin direction does not deviate drastically from the average value, or the exchange interaction is a long range interaction and many spins contribute to equation 1.15. If we replace each spin in 1.15 by its mean value, we will obtain [1]:

$$\mathbf{H}_{eff} = \mathbf{H} + \lambda\mathbf{M} \tag{1.16}$$

where:

$$\lambda = \frac{V}{N}\frac{J_0}{(g\mu_B)^2}, \qquad J_0 = \sum_R J(\mathbf{R})$$

Because magnetization is function of $\mathbf{H}_{eff}$, using 1.16 the susceptibility in the mean field approximation is given by:

$$\chi = \frac{\partial M}{\partial H} = \frac{\partial M_0}{\partial H_{eff}}\frac{\partial H_{eff}}{\partial H} = \chi_0\left(1 + \lambda\frac{\partial M}{\partial H}\right) = \chi_0(1 + \lambda\chi) \tag{1.17}$$

where χ_0 is susceptibility evaluated in the field $\mathbf{H}_{eff}$ and obeyed Curie's law. From this equation we can obtain the correction to Curie's law known as Curie–Weiss law:

$$\chi = \frac{C}{T - \lambda C} = \frac{C}{T - T_c} \tag{1.18}$$

where C is Curie's constant expressed by equation 1.13. Equation 1.18 differs from Curie's law for an ideal paramagnet only by denominator in which T was replaced by $T - T_c$. The Curie–Weiss law express the dominant correction to the hight–temperature Curie's law susceptibility, but near T_c measured susceptibility diverges as an inverse power of $T - T_c$ somewhere between $\frac{5}{4}$ and $\frac{3}{4}$.

Pauli paramagnetism

The contribution to the susceptibility due to conduction electrons in metals is [1]:

$$\chi = \mu_B^2 g(\varepsilon_F) \tag{1.19}$$

where μ_B is the Bohr magneton[1] and $g(\varepsilon_F)$ is the density of levels at the Fermi level.

The equation 1.19 is known as Pauli paramagnetic susceptibility. In contrast of paramagnetic materials, which obey Curie's law, the Pauli susceptibility is temperature independent. In free electron case the density of levels has form $g(\varepsilon_F) = mk_F/\hbar^2\pi^2$ and then we can estimate scale of Pauli susceptibility as $\chi_{Pauli} \approx 10^{-6}$ which is only minute size in compare with other susceptibilities mentioned above.

1.1.3 Magnetic interactions

Some type of materials at a critical temperature can get into magnetic ordered state. It happens, when ordering interactions tending to order magnetic moments become stronger than thermal fluctuations, which force a disorder of magnetic moments. It has been shown that in the most cases ordinary electrostatic electron–electron interaction combined with Pauli principle is responsible for magnetic ordering [1]. The magnetic dipole–dipole interaction and the spin orbit coupling are weak in compare with Coulomb interaction and in most theories of magnetism are ignored. However, dipole–dipole interactions are responsible for creating domains in the ferromagnetic ordered material.

There are three types of magnetic exchange interactions, which can be responsible for creation of magnetic ordered state:

[1] $\mu_B = \frac{e\hbar}{2mc}$

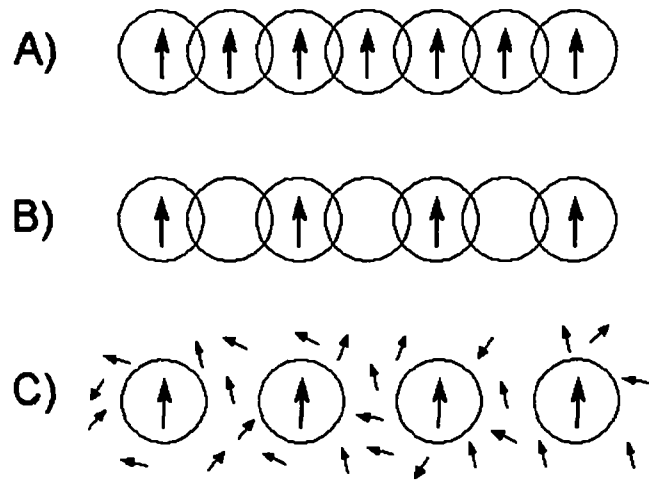

Figure 1.2: Basic types of magnetic interactions: a) direct exchange, b) indirect exchange c) RKKY interaction.

1. **Direct exchange** arises from the direct Coulomb interaction among electrons from the two ions. This type of interaction occurs in compounds with d–atoms in magnetic state, because d shells of neighboring atoms are considerably overlapped. Interaction is strong, but short–range, so is responsible for the high ordering temperature, but small effective moment.

2. **Indirect exchange** is typical for materials, in which the magnetic ions are separated by nonmagnetic ions. In this case exchange interaction is mediated via polarization of ligand states of nonmagnetic ions.

3. **Itinerant exchange** or also known as RKKY[2] interaction is mediated by conduction electrons. When conduction electron gets into strong magnetic field created by $4f$electrons (for example), it becomes polarized. When this polarized electron reach another atom earlier than it becomes depolarized, it will bring to this atom information of the spin orientation of the nearest atom and this way conduction electron mediates this interaction. The RKKY interaction have oscillating character, so this type of interaction can be responsible for ferromagnetic and also for antiferromagnetic ordering.

The second and the third type of interactions are weaker than direct interaction, but they are coupling moments over relatively large distances. The outline of some types of magnetic interactions is schematically sketched on in the figure 1.2.

[2]Named after Ruderman, Kittel, Kasuya and Yosida who have developed this model

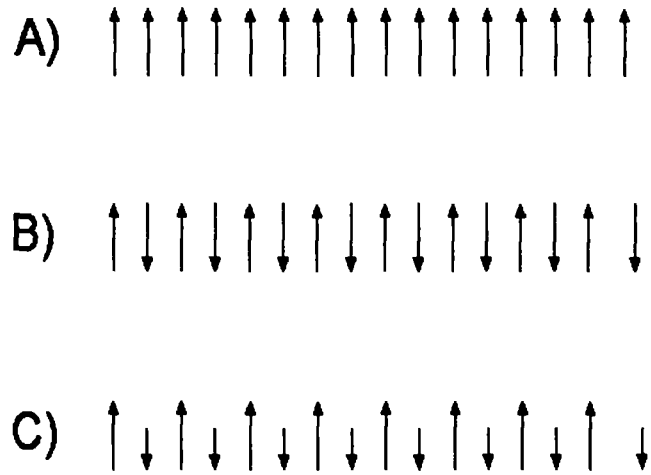

Figure 1.3: Basic types of magnetic ordering schemes on string of spins in plane: a) ferromagnetic coupling, b) antiferromagnetic coupling, c) ferrimagnetic coupling.

1.1.4 Magnetic structures

If in the solid is some type of magnetic interaction mentioned above, the solid will reach ordered state under condition that magnetic interaction is stronger than thermal fluctuations.

The individual magnetic moments in the ordered solid could be oriented parallel. In this case, in zero external field solid will have macroscopic bulk magnetization density known as *spontaneous magnetization*. This type of ordered state is described as *ferromagnetic*.

On the other hand, the magnetic moments can order antiparallel. For this kind of ordering we can always use Neel's theory of interpenetrating sublattices. This theory predict that solid can be always divided into finite number (in most cases 2) of interpenetrating sublattices. In each sublattice moments are ordered parallel to each other, but between sublattices there is antiparallel ordering. If in all sublattices are only ions with equal absolute value of their spins, there is no bulk magnetization density in the zero external field and so there is not spontaneous magnetization. This type of solid is known as *antiferromagnetic*.

Different case becomes, when in the different sublattices are different ions with different absolute value of their spins. Although the sublattices are orientated antiparallel, the spins are not compensated and there is (like in ferromagnets) spontaneous magnetization. This type of materials are called *ferrimagnets*, because after first observations, they were regarded to be ferromagnets with very strange temperature dependence of magnetization (which is depend on sum of magnetization for all sublattices).

A few types of magnetic ordering are illustrated schematically in the figure 1.3.

1.1.5 Itinerant, localized magnetism and mixed valence

An atom in a solid has a net magnetic moment in cases when an inner d or f electron shell is incomplete so that the individual electronic moments do not cancel completely. In the periodic table, there are five groups of elements in which this incomplete cancellation occurs: the iron group ($3d$), the palladium group ($4d$), the rare earth (or lanthanide) group ($4f$), the platinum group ($5d$), and the actinide group ($5f$). After a lot of years people can understand magnetic ordered systems only in two limited cases:

1. The itinerant (or weak ferromagnetic) electron magnetism for which the moments and their fluctuations are localized in k space, with their amplitudes being temperature dependent. This type of magnetism can be found for systems, where mainly d elements are in magnetic state.

2. The localized electron magnetism, for which the magnetic moments and their fluctuations are localized in real space (delocalized in k space), with their amplitudes being large and fixed. By this limit the magnetism of many $4f$ and $5f$ ions can be understood.

At first, we will deal with the magnetism of the delocalized (itinerant) band electrons. For these electrons the angular quantum number is no longer a sufficient description of their quantum state. Their properties can be described by a new quantum number, the electron momentum k. Each electronic state, which is now represented by a certain value of k, is occupied with electrons which differ pairwise in all their other quantum numbers so that the total angular momenta are always close to zero. In this situation the discrete energy levels and integer occupation numbers have now to be replaced by quasi-continuous energy levels. These are characterized by the respective k vector and a no longer integer occupation number given by the density of states. The electron states are given by plane Bloch waves they extend over the whole crystal, so possible magnetic moment created by these electrons is no longer localized at a certain atomic site but delocalized over the whole crystal. Also the energetic localization of the atomic–like energy states is broadened to a band state and appears to be energetically delocalized.

Most of the lanthanide ions in compound retain the localized atomic character of the $4f$ orbitals, so electronic properties of the $4f$ ions can be described within a single–ion Hamiltonian including the spin–orbit (SO), crystal field (CF), and exchange (EX) interactions:

$$H_R = H_{SO} + H_{CF} + H_{EX} \tag{1.20}$$

For most of the RE ions, the spin–orbit term dominates in the Hamiltonian of equation 1.20. Thus, the L–S coupling scheme remains valid, J is said to be a "good quantum number" and Hund's rules are valid.

The $4f$ orbital has a small radius and does not contribute directly to the bonding. In ordinary rare-earth compounds the $4f$ behaves as a localized orbital and the ordinary energy separation $E = E_n - E_{n-1}$ between configurations $4f^n$ and $4f^{n-1}$ is 5 – 10 eV. But for compounds with elements Ce, Sm, Eu, Tm

and Yb the separation can be only 0 – 2 eV [2]. In this case an interaction, which hybridizes the two configurations via a process where the conduction electrons hop on and off the rare-earth sites can cause them to fluctuate between $4f^n$ and $4f^{n-1}$ configurations. This leads to a quantum-mechanical ground state which contains the admixture of both configurations and compounds in which this phenomenon occurs are named mixed valence compounds [2].

1.2 Specific heat

1.2.1 Basic definitions

The specific heat is defined as the heat (δQ) required to rise the temperature (δT): $C_y = \delta Q/\delta T$, where y indicates the control parameters kept constant. This elementary definition works hand in hand with the development of the thermodynamics, because it is directly related to those parameters to be taken into account to describe the state of any physical system. In thermodynamics, specific heat at constant volume (C_v) is defined [3]:

$$C_v = T\sum\left(\frac{\partial S}{\partial T}\right)_v = \left(\frac{\partial U}{\partial T}\right)_v \tag{1.21}$$

Where T is thermodynamic temperature, S is entropy and U is energy. From the definition of specific heat, we can see that knowledge of specific heat provides a direct measurement of the entropy evolution ($S(T)$) over the system. The total specific heat of metallic system can be written as sum (1.22) of following contributions:

- lattice (phonon)(C_{ph})
- electronic (C_e)
- magnetic (C_{mag})
- nuclear (C_n)

Nuclear specific heat is related to hyperfine interaction between magnetic $4f$ shell and nuclear moment of magnetic $4f$ ion. This contribution to specific heat is dominant for $T < 0.5K$ and is usually recognized by a $C \propto T^{-2}$ dependence. At most cases we don't need to consider this contribution and for total specific heat we can write:

$$C_v = C_e + C_{ph} + C_{mag} \tag{1.22}$$

Total specific heat obtained from experiment have several main features:

1. At high temperatures, specific heat follows Dulong-Pettit's law, which says that for nonmagnetic metal the total molar specific heat per one atom is equal to three times gas constant.
2. At low temperatures, specific heat of phonons decreases and is proportional to T^3.

3. At zero temperature, specific heat is equal to zero.

4. If there is some phase transition of first kind at some temperature, the specific heat diverges at this temperature.

5. If there is the phase transition of second kind at some temperature, there jump in the specific heat is expected because of the change of the $\partial S/\partial T$ slope.

There are huge problems to separate different contributions from specific heat. For separating magnetic contribution from specific heat one can use comparative analysis of specific heat. The comparative analysis require to know specific heat of the isostructural nonmagnetic analogues, where only lattice and electron contributions are involved in specific heat. Parameters obtained from the analysis can be used as starting point for analysis of specific heat of magnetic compounds.

The volume of all real compounds is temperature dependent. So it's very difficult to measure specific heat at constant volume. In most cases, the specific heat at constant pressure (C_p) is measured. For solid matter C_v and C_p are related by equation [4]:

$$C_v - C_p = -\frac{9\alpha^2 V_m T}{\kappa} \tag{1.23}$$

Where α is coefficient of linear temperature expansion, V_m is molar volume and κ is coefficient of compressibility. For solid materials right side of equation (1.23) is small enough to neglect difference in values between C_v and C_p.

1.2.2 Phonon part

The thermal vibrations of atoms are not only simply independent oscillations of the individual atoms. Atoms in compound are tied up together, so oscillation of one atom affects another atoms. The collective vibrations of the crystal (phonons) are analyzed as the travelling waves, like ordinary sound waves though of much shorter wavelengths. These waves are quantized in momentum and energy. Four different kinds of phonons can be found in a crystal and are summarized in the Table 1.1. Longitudinal phonons means that atoms vibrate parallel to direction of wave and transversal phonons vibrate perpendicular to wave direction. In optical branch, atoms vibrate against each other, so mass centre don't move. If the atoms are electrically charged, we can produce this type of vibration by applying external electric field. On the other hand, acoustic phonons move in same direction, so mass centre moves.

In thermodynamic equilibrium at temperature T the occupancy of phonon mode gives Planck distribution function:

$$\langle n \rangle = \frac{1}{e^{\hbar\omega/k_B T} - 1} \tag{1.24}$$

where $\langle n \rangle$ means middle value in thermal equilibrium and k_B is Boltzmann constant.

There are two models, which are trying to solve phonon contribution to specific heat:

Phonon branch type	Vibration mode	No. of modes per unit cell
accoustic	longitudinal	3N
	transversal	for all acoustic
optical	longitudinal	(3n-3)N
	transversal	for all optical

Table 1.1: Phonon modes in crystal lattice. n is the number of atoms per unit cell, N is the number of wave vectors valid for one Brillouin zone.

Einstein model

Einstein tried to understand specific heat as vibrations of atoms. In his theory he suggested three postulates:

1. All atoms vibrate independent from all neighbor atoms.
2. The vibrations are isotopic. It means that all vibration modes are equivalent.
3. The vibrations can be expressed as vibrations of harmonic oscillators.

The thermal energy of 3N linear harmonic oscillators, which vibrate with the same frequency can be expressed as [3]:

$$U = N \langle n \rangle \hbar\omega = \frac{N\hbar\omega}{e^{\hbar\omega/k_B T} - 1} \tag{1.25}$$

We can define Einstein temperature Θ_E by equation:

$$\Theta_E = \frac{\hbar\omega}{k_B} \tag{1.26}$$

From the definition of specific heat (relation 1.21) we can then obtain phonon part of specific heat according to Einstein theory [3]:

$$C_E = N k_B \left(\frac{\Theta_E}{T}\right)^2 \frac{e^{\Theta_E/T}}{\left(e^{\Theta_E/T} - 1\right)^2} \tag{1.27}$$

There is question, whether Einstein theory of specific heat can describe obtained experimental results:

1. At $T = 0$ K the phonon contribution is equal to zero. Phonon contribution to specific heat according to Einstein theory is:

$$\lim_{T \to 0} C_E = 0 \tag{1.28}$$

2. For $T \to \infty$ the specific heat follows Dulong-Pettit's law. In the high temperature limit Einstein theory gives:

$$\lim_{T \to \infty} C_E = 3R \tag{1.29}$$

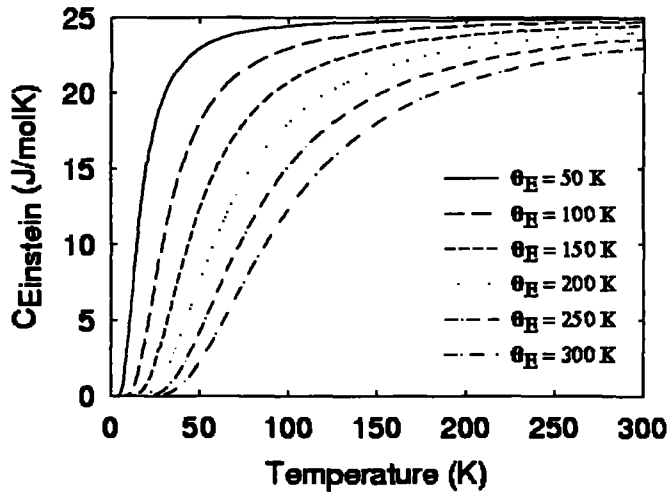

Figure 1.4: Theoretical dependency of specific heat on temperature according to Einstein theory

3. Experimentally was found that temperature dependence of specific heat at low temperature is proportional to T^3. For low temperature region in Einstein theory we can obtain:

$$C_E \approx \exp\left(\frac{\Theta_E}{T}\right) \tag{1.30}$$

As we can see, Einstein theory is good in both, zero temperature and high temperature limits, but at low temperature region fails. However, this model can be used for description of optical phonon contribution to specific heat. Theoretical temperature dependencies of specific heat due to Einstein theory for different Einstein temperatures are schematically plotted at figure 1.4.

Debye model

Debye assumed in his theory that atoms can vibrate with more than one frequency. In the thermal equilibrium set of oscillators, which vibrates with different frequencies ω_k have the energy [3]:

$$U = \int d\omega \mathscr{D}(\omega) n(\omega, T) \hbar\omega \tag{1.31}$$

where $\mathscr{D}(\omega)$ is density of vibrating modes and $n(\omega, T)$ is the Planck distribution function. The only problem in this equation is determining the $\mathscr{D}(\omega)$, which is done for example in [3]. Then we can define the Debye temperature (Θ_D) as:

$$\Theta_D = \frac{\hbar\omega_D}{k_B} \tag{1.32}$$

we can obtain relation for specific heat according to Debye theory [3]:

$$C_D = 9Nk_B\left(\frac{1}{x_D}\right)^3 \int_0^{x_D} dx \frac{x^4 e^x}{(e^x - 1)^2} \tag{1.33}$$

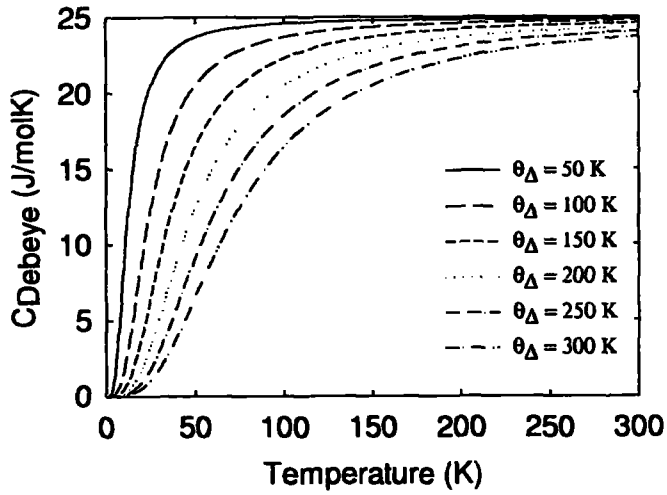

Figure 1.5: Theoretical dependency of specific heat on temperature according to Debye theory

Where $x_D = \Theta_D/T$. When we compare Debye theory of specific heat with experiments we will obtain:

1. For T $\rightarrow$ 0 the equation (1.33) converge to zero because:

$$\int_0^{x_D} dx \frac{x^4 e^x}{(e^x - 1)^2} \rightarrow 0 \tag{1.34}$$

2. At high temperatures equation(1.33) follows Dulong-Petit law:

$$\lim_{T \rightarrow \infty} C_D = 3NR \tag{1.35}$$

3. At low temperature region, one can approximate equation (1.33) by so called Debye T–cube law:

$$C_D \approx \frac{12\pi^4}{5} N k_B \left(\frac{T}{\Theta_D}\right)^3 = const.T^3 \tag{1.36}$$

So we can see that Debye theory of specific heat describes experiment better than Einstein theory. In practice, this theory is used to describe acoustic branches of phonon spectrum. Theoretical temperature dependencies of specific heat due to Debye theory for different Debye temperatures are schematically plotted in the figure 1.5.

Integral in equation 1.33 can not be solved analytically. On the other hand equation 1.33 can be replaced by form [5] with very good precision:

$$C_D = \frac{24.9416 + 0.05313x_D^2 + 9.85 \times 10^{-4} x_D^4 + 4.8 \times 10^{-7} x_D^6}{1 + 0.0521x_D^2 + 8.71 \times 10^{-4} x_D^4 + 4.56 \times 10^{-6} x_D^6 + 2 \times 10^{-8} x_D^8} \tag{1.37}$$

Anharmonic corrections to phonon spectrum

Both theories described above predict that atoms oscillate as harmonic oscillators. This postulate can be fulfil only at very low temperatures. At higher temperatures anharmonicity of vibrating atoms can play an important role and have to be taken into account for phonon part of specific heat. In this case optical branches of phonon spectrum are described by Einstein theory and acoustic branches of phonon spectrum are described by Debye theory [5]:

$$C_{ph} = R\left(\sum_{i=1}^{3n-3} \frac{1}{1-\alpha_{Ei}T} \frac{(\Theta_E/T)^2 \exp(\Theta_E/T)}{(\exp(\Theta_E/T)-1)^2} + \right. \tag{1.38}$$

$$\left. \frac{9}{1-\alpha_D T}\left(\frac{\Theta_D}{T}\right)^3 \int_0^{\Theta_D/T} \frac{x^4 e^x}{(e^x-1)^2}\right)$$

Where α_E and α_D are anharmonicity correction terms for optical, resp. acoustic branches of phonon spectrum. α_E and α_D are of the order $10^{-4}K^{-1}$. The anharmonicity takes place only at higher temperatures.

1.2.3 Electronic part

When a sample is heated from zero temperature to higher temperature, only small part of electrons near Fermi surface can obtain energy. Rising of total energy U of electronic system can be described as [3]:

$$U = \int_0^\infty dE\mathscr{D}(E)f(E)E - \int_0^{E_F} dE\mathscr{D}(E)E \tag{1.39}$$

where $f(E)$ is Fermi distribution function and $\mathscr{D}$(E) is number of states per energy. Then for the electronic contribution to specific heat we can obtain [3]:

$$C_e = \frac{1}{2}\pi^2 k_B^2 N \frac{T}{E_F} \tag{1.40}$$

Electronic contribution to specific heat is linear dependent on temperature. In most cases peoples link together all constants and use for electronic contribution to specific heat equation:

$$C_e = \gamma T \tag{1.41}$$

Coefficient γ has value from ones to tenths mJ/molK^2, however in heavy fermion systems γ have values up to thousands mJ/molK^2. Electronic contribution to specific heat is dominant for temperature region $0.5K < T < 4K$ in which phonon part of specific heat is almost equal to zero (because of T–cube law).

1.2.4 Magnetic part

As the specific heat is the second derivative of the free energy ($C_v = T\partial^2 G/\partial T^2$), the specific heat defines the order of the phase transition at the critical temperature ($T = T_{ord}$). In the case of a

RE	Ground-state term	CF splitting
Ce	$^2F_{5/2}$	3 Kramer's doublets
Pr	$^3H_4$	2 doublets and 5 singlets
Nd	$^4I_{9/2}$	5 Kramer's doublets
Sm	$^6H_{5/2}$	3 Kramer's doublets
Eu	$^7F_0$	1 singlet
Gd	$^8S_{7/2}$	symmetric state, no splitting supposed
Tb	$^7F_6$	3 doublets and 7 singlets
Dy	$^6H_{15/2}$	8 Kramer's doublets
Ho	$^5I_8$	4 doublets and 9 singlets
Er	$^4I_{15/2}$	8 Kramer's doublets
Tm	$^3H_6$	3 doublets and 7 singlets
Yb	$^2F_{7/2}$	4 Kramer's doublets

Table 1.2: Ground state splitting caused by tetragonal crystal field of RE^{3+} ions.

first–order transition (for example paramagnetic $\leftrightarrow$ ferromagnetic transition) the discontinuity in $S(T)$ is reflected in $C_p(T)$ as a divergence at T_{ord}. In a second–order transition a jump in $C_p(T)$ appears, because of the change of the dS/dT slope. The temperature dependence of $C_p(T)$ close to the transition provides useful information about the microscopic nature of the transition (e.g. dimensionality).

In a mean field theory of the magnetic transitions the contribution to the specific heat due to magnetic transition ($\Delta C_m(T_{ord})$) depends on the momentum J according to [6]:

$$\Delta C_m(T_{ord}) = 2.5R\left[(2J-1)^2+1\right] \tag{1.42}$$

and the entropy related with the magnetic transition is given by:

$$\Delta S_m = R\ln(2J+1) \tag{1.43}$$

If in specific heat a discontinuity is only forced by the first order transition, the total entropy will not exceed $\Delta S_m = R\ln(2J+1)$.

Schottky anomaly

Frequent anomaly, which is observed in specific heat measurements is the so–called Schottky anomaly. This anomaly is related to the thermal excitations in a level system split by Δ caused by removing $(2J+1)$-fold degeneracy of ground state multiplet by crystal field. Because the thermal population of the levels is governed by Maxwell–Boltzmann statistics, the contribution to specific heat in paramagnetic

state can be expressed as a Schottky contribution [7]:

$$C_{sch} = \frac{R}{T^2}\left[\frac{\sum_{i=0}^{n}\Delta_i^2 \exp\left(-\Delta_i/T\right)}{\sum_{i=0}^{n}\exp\left(-\Delta_i/T\right)} - \left(\frac{\sum_{i=0}^{n}\Delta_i \exp\left(-\Delta_i/T\right)}{\sum_{i=0}^{n}\exp\left(-\Delta_i/T\right)}\right)^2\right] \tag{1.44}$$

Schottky anomalies are well observed when their respective characteristic energies (or associated gaps Δ) are about $k_B\Delta < 20K$. Two theorems deals about lifting degeneracy by crystal field:

Kramers theorem: For odd-electron systems (Kramers ions) there is a remaining twofold degeneracy which cannot be removed by any electric fields. The entropy of a Kramers ion is at least $S = k_B \ln 2$ at temperatures approaching absolute zero. This degeneracy thus must necessarily be removed by some mechanism if the third law of thermodynamics is to retain its validity.

The Jahn–Teller theorem: Any atom in a solid with ground state degeneracy of non–Kramers type may lift this degeneracy by lowering its symmetry.

The removing degeneracy by crystal field for $4f$ ions is summarized in table 1.2.

1.3 Electric transport

1.3.1 Basic definitions

When we apply voltage (U) between two ends of a material with free charge carriers, we can observe electric current (I) proportional to applied field in direction of applied field. This can be described by Ohm's law:

$$I = \frac{U}{R} \tag{1.45}$$

where R is electric resistivity. To avoid problems with volume parameters of the sample we can define specific electric resistivity (ρ):

$$R = \rho\frac{l}{S} \tag{1.46}$$

where l is length of sample between voltage contacts and S is cross section of sample.

Matthiessen's rule

If there are two or more independent scattering mechanisms, the probability that electron scatters by any of these scattering mechanisms can be described as summation of this probabilities. So for total resistivity we can write the formula known as Matthiessen's rule:

$$\rho = \rho_0 + \rho_{phon} + \rho_m \tag{1.47}$$

where ρ_0 is the potential scattering, ρ_{phon} is the phonon scattering and ρ_m is the magnetic scattering. The potential, phonon and magnetic scattering will be discussed.

Potential scattering

Because of these scattering processes are elastic, no energy transfer between the conduction–electron system and the scatterer takes place. Such scattering may occur on dislocations, foreign atoms and grain boundaries. The transport coefficients due to this kind of interaction are given by:

$$\rho_0(T) = C \tag{1.48}$$

where C is temperature independent constant. ρ_0 can be extracted by extrapolating temperature dependency of resistivity to zero temperature in which all other contributions to resistivity are equal to zero.

Phonon scattering

Using the Debye model to describe the lattice dynamics, the simplest results for the transport coefficients are given by Bloch–Grüneisen formula [8]:

$$\rho_{phon} = 4C_{phon}\left(\frac{T}{\Theta_D}\right)^5 \int_0^{\Theta_D/T} dx \frac{x^5}{(e^x - 1)(1 - e^{-x})} \tag{1.49}$$

where C_{phon} is temperature independent parameter, which contains constants for electron–electron coupling and atom masses. Θ_D is Debye temperature described in section 1.2.2. We can approximate equation 1.49 for the low and the high temperature limits by:

1. For low temperature region where $T \ll \Theta_D$:

$$\rho_{phon} \approx T^5$$

2. For high temperature region where $T \geq \Theta_D$:

$$\rho \approx T$$

Which provides very good agreement with experiments.

Spin–dependent scattering mechanism

The contribution to the total electrical resistivity due to spin–dependent scattering mechanism depends strongly on whether the material is magnetically ordered or is in the paramagnetic state.

If the material is in the paramagnetic state the magnetic moments in the material are disordered and the contribution to the electrical resistivity is temperature independent:

$$\rho_{spd} = C_m \tag{1.50}$$

The description of magnetic scattering under ordering temperature was done for example by Andersen [9]. He tried to describe decrease of resistance due to electron–magnon interaction in Tb by term:

$$\rho_m = \rho_0 + aT^2 + ET\left(1 + \frac{2T}{\Delta}\right)\exp\left(\frac{-\Delta}{T}\right) \tag{1.51}$$

where all constants are temperature independent ad E depends on electron–magnon coupling constant and Δ represents gap in the dispersion relation of ferromagnetic magnons.

1.3.2 Electric transport under external magnetic field

Now, let us consider that electron is affected by combined influence of externally applied electric and magnetic fields. In this case, we have to consider that the conductivity is a tensor and the Ohm's law can be written as:

$$\vec{I} = \overleftrightarrow{\sigma}\,(T, \vec{B}) \cdot \vec{E} \tag{1.52}$$

For the material with the cubic symmetry and for field $\vec{B} = (0, 0, B)$ the resistivity tensor is given as:

$$\overleftrightarrow{\rho}\,(\vec{B}) = \begin{pmatrix} \rho_\perp(B) & \rho_H(B) & 0 \\ -\rho_H(B) & \rho_\perp(B) & 0 \\ 0 & 0 & \rho_\parallel(B) \end{pmatrix} \tag{1.53}$$

where $\rho_\perp$ and $\rho_\parallel$ are resistivity in perpendicular, resp. parallel direction of magnetic field to electric current and ρ_H is the Hall resistivity. The magnetoresistance and the Hall resistivity are discussed in sections below.

Magnetoresistance

When we apply electric and magnetic force on free electron, the electron will be affected by Lorentz force:

$$\vec{F}_L = -e(\vec{E} + \vec{v} \times \vec{B}) \tag{1.54}$$

where $\vec{v}$ is velocity of the electron and $\vec{B}$ is applied magnetic field. From equation 1.54 we can see that magnetic field does not affect absolute value of velocity of electron, but curves its trajectory (in the case that $\vec{v}$ is not parallel, neither antiparallel to $\vec{B}$). This mechanism always increases the resistivity with the field and is called "normal magnetoresistance".

The situation is more complex in compounds where the ions bear magnetic moments, since spin–dependent scattering processes are also involved (below as well as above the magnetic ordering temperature).

In the case of ferromagnet the local minimum is observed on temperature dependence of relative magnetoresistance at transition temperature. The properties of this minimum are [6]:

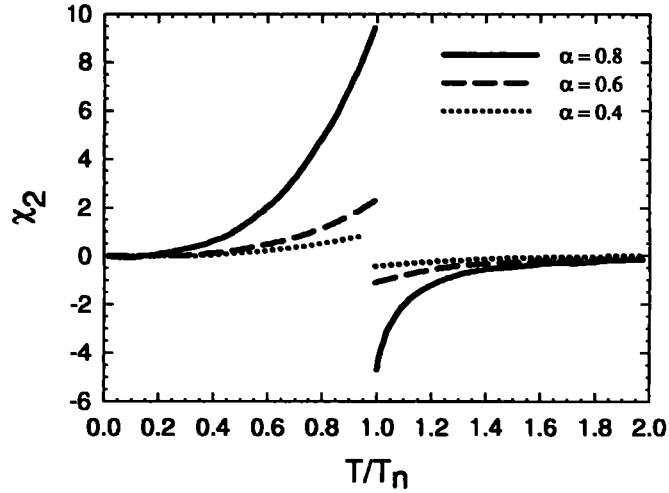

Figure 1.6: Temperature variation of the function $\chi_2(T/T_N)$ calculated for Neel temperature 50 K [10].

1. For paramagnetic region where $T \gg T_c$ and under condition that $(T/T_c - 1) \gg C_2$:

$$\frac{\Delta\rho_m}{\rho_{spd}} = -C_1 \frac{C_2^2}{(T/T_c - 1)^2} \tag{1.55}$$

where:

$$C_1 = \frac{4J^2 + J + 1}{9}; \qquad C_2 = \frac{g\mu_B}{2k_B T_c} B$$

2. Magnetically ordered region where $T < T_c$ and $1 \gg (1 - T/T_c)^3 \gg C_2^2$:

$$\frac{\Delta\rho_m}{\rho_{spd}} = -C_1 C_2 \left(\frac{C_3}{1 - T/T_c}\right)^{1/2} \tag{1.56}$$

where:

$$C_3 = \frac{2(2J^2 + 2J + 1)}{15}$$

In the antiferromagnet, there is different situation because of two ferromagnetic sublattices. If the field strength B necessary to induce a ferromagnetic spin arrangement exceeds the critical field, $\Delta\rho_m/\rho_{spd}$ starts to decrease as in a ferromagnet. But for $T < T_N$ according to [10] the temperature dependence of $\Delta\rho_m/\rho_{spd}$ is given by:

$$\frac{\Delta\rho_m}{\rho_{spd}} = \chi_2(T/T_N) \frac{g\mu_B}{2k_B T_N} B \tag{1.57}$$

where the function χ_2 describes the relative strength of the nearest–neighbor interaction in the magnetic lattice. This function is plotted on figure 1.6.

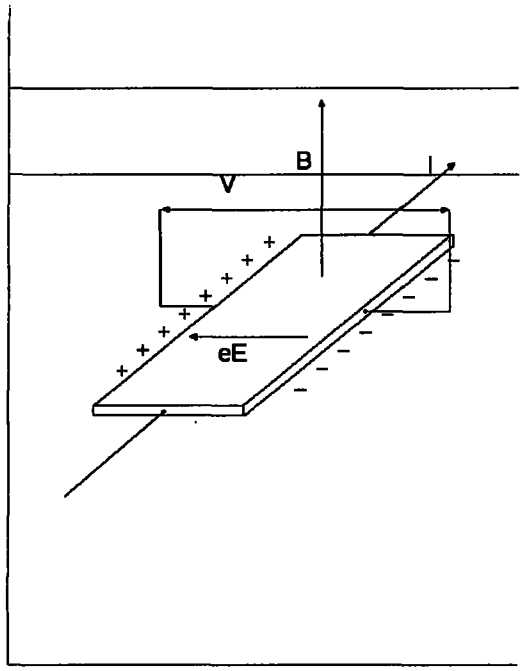

Figure 1.7: Experimental geometry for measurement of the Hall effect.

Hall effect

Applied magnetic field can curve trajectory of electron. We can measure voltage perpendicular to current direction and perpendicular to applied external magnetic field $\vec{B}$. Geometry of this experiment is sketched on figure 1.7. In this case transverse field (E_y) will appear as [11]:

$$E_y = R_H \vec{B} \times \vec{j} \tag{1.58}$$

where R_H is the Hall coefficient and $\vec{j}$ is current density. R_H measured on a thin plate with a thickness of d can be determined experimentally as:

$$R_H = \frac{V_y d}{IB} \tag{1.59}$$

where V_y is the transverse voltage and I is the current.

The general expression for the Hall resistivity in magnetic materials is given empirically as [11]:

$$\rho_H = R_H B + R_S M \tag{1.60}$$

where R_H is called the normal Hall coefficient and second term is the anomalous Hall resistivity.

Chapter 2

Experimental

2.1 RET_2X_2 compounds

During the last years the intermetallic compounds with stoichiometric formula RET_2X_2[1] were systematically studied. A very interesting phenomena, like superconductivity and heavy–fermion behavior ($CeCu_2Si_2$ [12]), spin glass behavior ($PrAu_2Si_2$ [13]), mixed valence (CeM_2Si_2 where M = Mn, Fe, Co, Ni [14, 15, 16]), incommensurate modulated magnetic structure (for example $PrNi_2Si_2$ [17]), change of magnetic structure from incommensurate magnetic structure to simple antiferromagnetic structure ($TbNi_2Si_2$ [18]) and anomalous Hall effect due to skew scattering ($CeRu_2Si_2$ [19]) were observed.

The RET_2X_2 compounds can crystallize in three possible groups of different structure types:

1. The $ThCr_2Si_2$–type body centered tetragonal structure with space group $I4/mmm$. This type can be expressed by RE–X–T–X–RE–X–T–X–RE alternating layers perpendicular to the $c-$axis.

2. $CaBe_2Ge_2$–type primitive tetragonal structure (space group $P4/nmm$). In this structure alternation of layers perpendicular to $c-$axis is RE–T–X–T–RE–X–T–X–RE. Layered crystal structures of these compounds is strongly reflected in their magnetic properties.

3. $CeAl_2Si_2$ structure with space group $P\bar{3}ml$. this structure can be derived from hexagonal close packed structure, in which half of the octahedral and half of the tetrahedral holes are occupied in an ordered manner.

For magnetic behavior it is important that transition metals carry no magnetic moment. Only *4f* shell of rare earth atom, which remains localized, carries magnetic moment. The *5d* and *6s* electrons are involved in the conduction band. *4f* wave functions carry high magnetic moment, so can polarize *5d* wave functions. The *3d* wave functions of transition metal hybridize with polarized *5d* wave functions of rare earth. This is an origin of indirect exchange interaction in this type of compounds. Another

[1] In this formula RE is the rare-earth element including Y and Sc, T is a transition *3d*, *4d* or *5d* element and X is the main group element from the boron, carbon or nitrogen group.

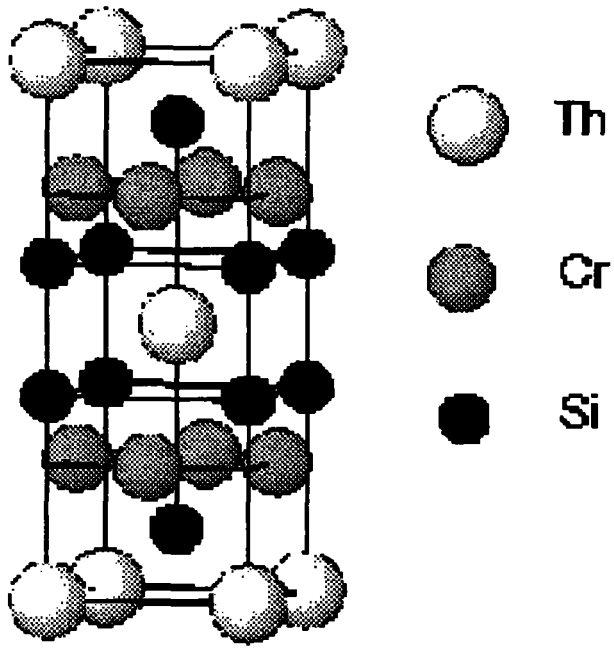

Figure 2.1: $ThCr_2Si_2$ type crystal structure.

exchange interaction is interaction between $4f$ shells mediated by conduction electrons (described by e.g. RKKY interaction).

2.1.1 $REFe_2Si_2$ compounds

The $REFe_2Si_2$ compounds crystallize in the $ThCr_2Si_2$–type crystal structure (fig. 2.1). In the elementary cell, rare earth atoms occupy (0 0 0)site, iron atoms occupy (0 1/2 1/4) site and silicon atoms occupy (0 0 z) site, respectively, where z is the free parameter. Lattice parameters are summarized in table 2.1.

Lanthanum has no magnetic moment, so $LaFe_2Si_2$ can be used in the comparative analysis of specific heat to extract the magnetic part of specific heat. The specific heat of polycrystalline $LaFe_2Si_2$ was measured and carefully analyzed in [20]. The phonon contribution to specific heat was described by three acoustic branches with $\Theta_D = 204 \pm 5$ K and 12 optical branches. The optical branches were considered as 4–times degenerated with the Einstein temperatures $\Theta_E = 202 \pm 5, 353 \pm 7$ and 505 ± 9 K. The electronic contribution to specific heat was described using $\gamma = 22.7 \pm 0.2$ mJmol^{-1}K^{-2}.

The $CeFe_2Si_2$ is a mixed valence system [14, 15]. It was found that the average valence of Ce in

compound	a (Å)	c Å	Ref.	Ground state	$T_{ord}(K)$	Ref.
$LaFe_2Si_2$	3.9762	10.0023	[20]	Pauli paramag.	—	[21]
$CeFe_2Si_2$	3.991	9.881	[22]	Mixed valence		[15]
$PrFe_2Si_2$	4.0037	10.0542	[20]	AF	7.7	[23]
$NdFe_2Si_2$	3.9899	10.0382	[20]	AF	15.6	[24]
$SmFe_2Si_2$	3.952	9.985	[22]			
$GdFe_2Si_2$	3.940	9.974	[24]	AF	8	[25]
$TbFe_2Si_2$	3.925	10.0088	[26]	AF	6.5	[26]
$DyFe_2Si_2$	3.896	9.890	[24]	AF	3.8	[27]
$HoFe_2Si_2$				AF	2.2	[25]
$ErFe_2Si_2$	3.888	9.897	[22]	AF	2.6	[25]
$TmFe_2Si_2$	3.882	9.889	[22]			

Table 2.1: Lattice parameters and ordered magnetic state of $REFe_2Si_2$ compounds.

$CeFe_2Si_2$ is about 3.3 at room temperature and decreases with increasing temperature. Temperature dependence of resistivity was measured in [15]. The resistivity follows equation 1.49 in the temperature interval 4 – 270 K.

The analysis of specific heat was done for the single crystal of $PrFe_2Si_2$ and is reported in [20]. The sharp peak found on the temperature dependence of specific heat at about T = 7 K was assigned to a magnetic phase transition. The following dull maximum was attributed to a Schottky anomaly. Heat capacity data in paramagnetic region were analyzed in order to extract crystal–field splitting. In the case of $PrFe_2Si_2$ the crystal field splits the ground–state $^3H_4$ multiplet of Pr^{3+} into 9 singlets with energy distances from the ground–state level as $\Delta = 28.5 \pm 0.3, 136 \pm 2, 230 \pm 5, 370 \pm 7, 480 \pm 8, 505 \pm 10, 540 \pm 15$ and 600 ± 15 K. The susceptibility, neutron diffraction and the Mössbauer spectroscopy measurements of $PrFe_2Si_2$ are reported in [28, 29]. It was found that the compound is the type II (+ + − −) antiferromagnet (AF) and the c–axis is the easy magnetization direction. No magnetic saturation was reached at the field of 50 kGauss [29]. From neutron diffraction [28] the effective magnetic moment was determinated on $\mu_{eff} = 1.42(5)\mu_B$ at 1.3 K, $\mu_{eff} = 2.43\mu_B$ at 5 K.

The specific heat analysis of the $NdFe_2Si_2$ is reported in [20]. The sharp peak found at T = 12 K was assigned to the magnetic phase transition. It was found that the crystal field splits the ground–state $^4I_{9/2}$ multiplet into 5 Kramers doublets with energy distances from the ground–state level as $\Delta = 93 \pm 5, 135 \pm 5, 215 \pm 10$ and 280 ± 10 K. The magnetization measurements on $NdFe_2Si_2$ crystal are reported in [30]. The cusp at around 13.7 K was found on the temperature dependence of magnetization,

which was assigned to the magnetic phase transition. The uniaxial magnetic anisotropy was observed with the $c-$axis as the easy axis of magnetization. The metamagnetic transition was found on the magnetization curves in the external field $B = 3.45$ T for the $a-$axis and in the field $B = 1.14$ T for the $c-$axis. The magnetization curves exhibit saturation above the metamagnetic transition for the $c-$axis. On the other hand, for the $a-$axis the magnetization does not saturate in fields up to 10 T.

For $SmFe_2Si_2$ only the temperature dependence of magnetization was measured on a polycrystal and no sign of magnetic phase transition was found down to 4 K [24].

A Mössbauer spectrum of the ^{57}Fe isotope was measured on $GdFe_2Si_2$ compound at 300 K [31]. Claiming that internal field acting on ^{57}Fe is less than 5 kOe. The temperature dependence of the magnetization indicates that there is AF ordering in temperature below $T_N = 8$ K [25].

On polycrystalline $TbFe_2Si_2$ the magnetic properties and the temperature dependence of resistivity were measured [26]. Two anomalies (at 6.5 K and 180 K) were observed on the temperature dependence of $1/\chi$. The anomaly at 6.5 K was assigned to the magnetic phase transition. From the slope of $1/\chi(T)$ between temperatures 180 and 290 K the magnetic moment was calculated. It was determined that the effective moment is between 7 and 9 μ_B. Deviation of $1/\chi(T)$ from linearity found below 180 K point to the fact that there is an extra spin magnetic moment added to Curie–Weiss behavior. Very unusual field dependence of magnetization at temperatures 2 and 5 K (up to 30 kOe) were found. The field dependence of magnetization above 50 K seemed to be similar as in paramagnetic state. The resistivity measurements showed that temperature dependence of resistivity follow equation 1.49 in the temperature interval 2 – 250 K. The neutron diffraction study revealed that the magnetic structure is incommensurate with the crystallographic unit cell [32].

2.2 Used experimental techniques

2.2.1 Growing crystals by Czochralski method

Crystal growth by Czochralski method is one of the two most spread methods used for preparation of bulk single crystals from melt. The apparatus usually consists of a crucible, pulling head, furnace and a sample chamber. In our case, the charge with mass of about 7 g was placed in water cooled copper crucible, which is able to rotate. The heat necessary for the melting of the compound is supplied by three arcs. To avoid the outgassing from the walls and contamination of the melt in the crystal growth process, the sample chamber is evacuated and backed usually overnight before the start of the crystal growth. Then the chamber is filled with the Ar protective atmosphere. Prior to the crystal growth the compound is melted and homogenized by re–melting. Then a rotating seed of grown crystal (if the matching crystal is accessible) or tungsten rod is immersed to the melt and then slowly pulled up. The direction of the seed rotation is opposite to the rotation of the crucible. Basic principle of this method is gradual growth of crystal grain size and simultaneous reduction of the number of the grains. It is

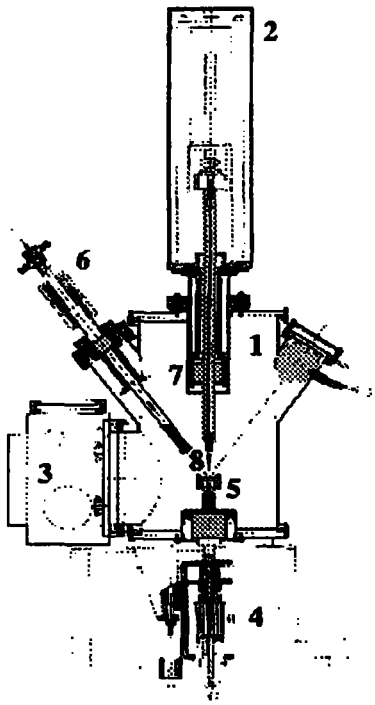

Figure 2.2: Schematic cross-section of a tri-arc furnace. Only one arc is shown. 1: sample chamber, 2: pulling head, 3: glow box, 4: rotating mechanism of crucible, 5: crucible, 6: torch, 7: ferrofluid, 8: sample.

possible to propagate one crystalline grain by reduction of the pulling ingot diameter (so called necking). The more slowly the ingot is necked, the better crystal and lower mosaicity is achieved. The thinner the neck, the higher probability that only one crystalline grain is propagating below the neck, but the higher probability that the ingot can break during pulling. The neck thickness is typically about 1 mm. After necking, the ingot diameter is increased to the required dimensions by decreasing the arc current and by decreasing the pulling speed. When a satisfactorily large piece of material is grown, the crystal is separated from the melt by increasing pulling speed and increasing arc currents.

The tri-arc furnace for growing crystals by the Czochralski method in which the crystals were grown has been designed and built in cooperation with VAKUUM Praha company as an improved version of the tri-arc furnace of the van der Waals-Zeeman laboratory, Amsterdam [33]. The furnace is sketched on figure 2.2.

2.2.2 X-ray analysis

In case of X-ray diffraction on the ideal three dimensional crystal lattice the diffraction have to fulfill Laue's diffraction conditions [34]:

$$\begin{aligned} \vec{a}(\vec{s}-\vec{s}_0) &= h\lambda \\ \vec{b}(\vec{s}-\vec{s}_0) &= k\lambda \\ \vec{c}(\vec{s}-\vec{s}_0) &= l\lambda \end{aligned} \tag{2.1}$$

Laue method

The aim of this method is to determine the symmetry and orientation of a single–crystalline sample or to determine the number of crystallites in the sample, respectively.

In our case we used "reflection geometry" which means that primary beam first crosses through the film then hit the sample and we detect backscattered diffraction on the film.

When the sample is the single crystal, conditions 2.2 are fulfilled only for exact angles. As a result we can observe spots on the film (each from different system of planes *hkl*). From the position of the spots we can find out the orientation of the sample. There are several programs, which can help with the orientation of the samples. One of them is Orient Express [35].

The disadvantage of X-ray is its small penetration depth. So by the Laue method we can obtain information about orientation and number of the grains only from the surface of the sample, not from the bulk.

Powder diffraction

In the ideal powder all grains are randomly oriented. The very frequently used geometry for powder diffraction is Bragg–Brentano configuration [34] and by performing 2Θ scan in this configuration we can obtain powder diffraction spectra (for example see figure 2.7 in section 2.3). Then, when the crystallographic model of the sample is known, the Rietveld analysis[2] [38] can be used to refine the crystallographic parameters and eventually to determine impurities (the sensitivity of the method for determination impurities is about 3%).

One of the program for the Rietveld fitting is *Fullprof* [36] together with its graphical interface for Windows named *Winplotr* [37].

[2]Rietveld minimize function $m = \sum_i w_i(y_i - y_{ci})^2$, where w_i is the weight assigned to the individual step intensity, y_i is the observed intensity at the i-th step and y_{ci} is the calculated intensity at the i-th step of pattern.

2.2.3 Magnetization measurements

Extraction magnetometer

The extraction magnetometer is based on extracting sample from the detection coils. Then, according to Faraday's law[3] the voltage on the detection coils can be observed. The magnetic measurements were performed on PPMS measurement system. In this system the detection coils are in the first–order gradiometer configuration, which means that there are two sets of counterwound copper coils connected in the series. The velocity, of the sample extraction from detection coils is 1 m/s. The sensitivity of the system is better than 2×10^{-10} Am^2.

Demagnetizing factor

When we insert a sample into a magnetic field, the intensity of magnetic field around the sample and inside the sample will change. Generally the internal magnetic field will be smaller than external field by demagnetizing field:

$$H_i = H_e - H_d \tag{2.2}$$

where H_i is internal field; H_e is external field and H_d is demagnetizing field which is proportional to magnetization:

$$H_d = DM \tag{2.3}$$

where D is the demagnetizing factor along the measured direction and M is magnetization. Let us consider revolting ellipsoid with rotational axis defined as a and defined parameter $p = a/b$. If we suppose that $p > 1$ then we can get for demagnetizing factor along $a-$axis [39]:

$$D_a = \frac{1}{p^2-1}\left\{\frac{p}{\sqrt{p^2-1}}\ln\left(p+\sqrt{p^2-1}\right)-1\right\} \tag{2.4}$$

On the other hand, the sum of demagnetizing factors along all principal axes is 1. In case of revolting ellipsoids $b = c$, so:

$$D_b = \frac{1-D_a}{2} \tag{2.5}$$

2.2.4 Specific heat measurements

Specific heat measurements were performed by PPMS system [40]. PPMS use for determining the specific heat fitting the whole temperature response of a heat-pulse calorimeter technique. The details of this technique are referred in [41]. The supposed heat flow and the experimental puck used for measurements are sketched on fig. 2.3.

The initial values, which we used for the theoretical fitting of phonon contribution to specific heat was obtained from polycrystalline $LaFe_2Si_2$ compound. To simplify calculations we decided to divide optical

[3]Faraday's law: $\oint_c \vec{E}\cdot d\vec{l} = -\frac{\partial}{\partial t}\int_S \vec{B}\cdot d\vec{S}$

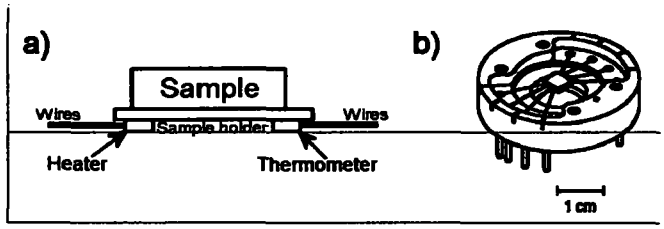

Figure 2.3: a) The side view of the sample holder of heat capacity puck in PPMS system. b) The sketch of heat capacity puck frame in PPMS. The plate in the middle of the puck frame is the sample holder.

branches to three groups with 2, 4 and 6 fold degeneration respectively. The degree of degeneration was derived from the symmetry of the space group $I4/mmm$.

2.2.5 Electric transport measurements

The standard experimental technique for electric transport measurements is the four–probe AC method. The geometry of contacts in this method is sketched in the figure 2.4. This method is very effective in eliminating contribution of contacts to measured signal [39].

In this work the resistivity measurements were performed on the PPMS (Quantum design) measurement system [40] in constant current mode. The sketch of used puck in PPMS for electric transport measurements is shown in figure 2.5. The applied AC current was typically of the amplitude 10 mA and frequency 71 Hz, respectively. The duration of measured pulse was typically 0.5 second. The contacts were made by silver paint and resistivity of contacts was in most cases less than 1 Ω. The main contribution to the absolute error of the measurement was the error in determining the sample cross section and the distance between the voltage contacts. The absolute error in geometrical parameters determination was about 0.05 mm.

From resistivity data we can determine residual resistivity ratio (RRR), which can give us information about the quality of the single crystal. RRR can be obtained as a ratio of the electrical resistivity

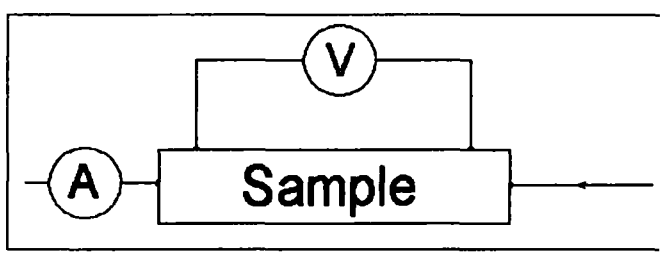

Figure 2.4: Experimental configuration of contacts in four–probe method.

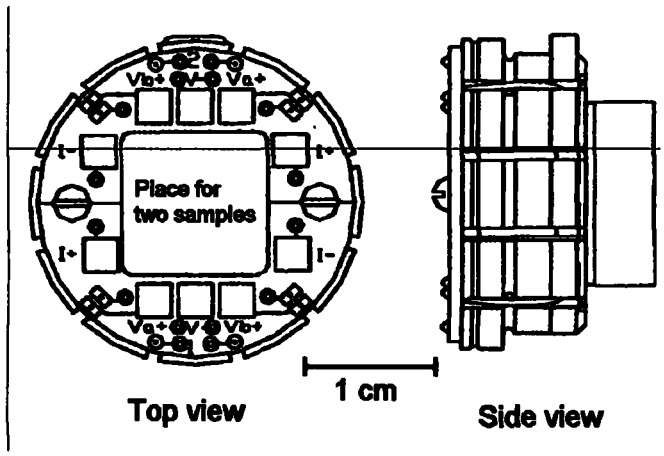

Figure 2.5: The sketch of puck used in PPMS for electric transport measurements.

at room and at the lowest available temperature:

$$RRR = \frac{\rho_{T_{\text{maximum}}}}{\rho_{T_{\text{minimum}}}} \tag{2.6}$$

The *RRR* as a ratio of two experimental values is not affected by the error due to geometry of sample. A good single crystal should have the *RRR* over 30.

2.3 Obtained experimental results

2.3.1 Sample preparation and characterization

For the sample preparation we used typically about seven grams of a charge consisting of the stoichiometric composition of the elemental constituents with the nominal purity: Fe: 99.98%, Si: 99.999 % and Rare earth: 99.9 %. All samples used for measurements were grown by the modified Czochralski pulling technique (see section 2.2.1) with growing speed 6 – 8 mm/hour. The grown crystals were about 3.5 cm long with a maximal diameter of 4 mm. The example of grown crystal is in the figure 2.6. The quality of crystals was checked by Laue pattern. The other-phase-impurities and lattice parameters were determined from the powder X-ray diffraction on the pulverized piece from the grown ingot. Good crystallinity of all crystals was confirmed by the X-ray Laue patterns. For Rietveld analysis we used *Fullprof* program [36]. The Rietveld analysis of the powder diffraction pattern yielded no detection of any traces of foreign impurities within the sensitivity of the method (3 %). The example of refined structure is shown on figure 2.7 and the refined structure parameters are summarized in the table 2.2.

By extrapolating linear part of magnetization curves of hard-axis data a small amount of ferromagnetic impurity was detected by magnetic measurements. Assuming that this impurity is Fe-Si or Fe_2O_3

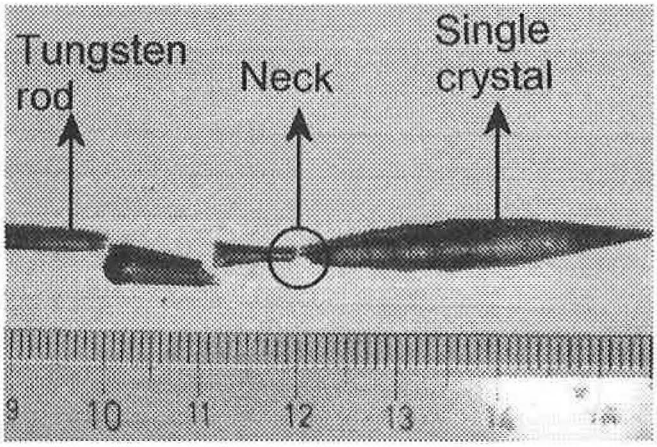

Figure 2.6: Single crystal of $DyFe_2Si_2$ grown by Czochralski method.

Compound	a (Å)	c (Å)	z (relative)	RRR $a-$axis	RRR $c-$axis
$PrFe_2Si_2$	4.0037	10.0542	0.3700	6.9	7.5
$TbFe_2Si_2$	3.9195	9.9594	0.3737	5.1	6.8
$GdFe_2Si_2$	3.9400	9.9939	0.3745	7.3	5.9

Table 2.2: The refined crystallographic parameters and RRR (can be understand as quality index of the crystal) for the studied $REFe_2Si_2$ compounds.

phase with the saturated magnetization about 2 μ_B/f.u. we can estimate the amount of this impurity as less then 0.2 %.

The easy-growth axis of the crystal is in basal plane. The resulting crystals are very brittle and in all cases the plane perpendicular to the $c-$axis is an easy cleaving plane. Because of this, it was very difficult to prepare samples for measurement along the $c-$axis. Along the $c-$axis the error in electric transport measurements is almost 4 times higher than along the $a-$axis.

2.3.2 Magnetic properties.

$PrFe_2Si_2$

Magnetization measurements of $PrFe_2Si_2$ revealed strong uniaxial anisotropy. The easy axis of magnetization is the $c-$axis (see fig. 2.8). The signal along $a-$axis is weak and linear up to field 9 T. The measurements along $c-$axis shows hysteresis up to the field $B = 14$ T. The hysteresis can be observable even in paramagnetic region. The magnetic moment in 14 T is $\mu = 2.25\mu_B$/f.u. which is less than magnetic moment of Pr^{3+} ion (3.5 μ_B).

From the temperature dependence of susceptibility measured along $c-$axis (fig. 2.10) we can determine the transition temperature as $T_N = 7.2$ K. The inverse-susceptibility plot shows that $PrFe_2Si_2$ doesn't obey the Curie-Weiss law. On the temperature dependence of the susceptibility measured along $a-$axis (fig. 2.9) we can see some additional peak at about 54 K, which can be eliminated by applied magnetic field. The scattering of data at higher temperatures is due to low signal (near to maximal resolution of the apparatus) from the sample.

$TbFe_2Si_2$

The low-temperature magnetization curves of $TbFe_2Si_2$ show large uniaxial magnetocrystalline anisotropy with the $c-$axis as an easy axis of magnetization. The magnetization along the $c-$axis saturates towards the value $\mu = 9\mu_B$/f.u., which is very close to the moment of the free Tb^{3+} ion (9.5 μ_B). In the case of the $a-$axis (fig. 2.11), the magnetization is almost linear, not exceeding $\mu = 0.5\mu_B$/f.u. in 5 T.

Closer inspection of the $c-$axis magnetization curves at temperatures below 5 K reveals that there is a metamagnetic transition starting at the field $\mu_0 H = 0.5$ T. To emphasize the effect, Arrot-plots (fig. 2.12 and fig. 2.13) were constructed from the magnetization data. The Arrot-plots for temperatures below 5 K clearly show the typical shape of an antiferromagnet with the metamagnetic transition.

The temperature dependence of inverse magnetic susceptibility shows strong anisotropy (fig. 2.14). Even at temperature $T = 300$ K the slopes and the values of inverse susceptibility measured along different axes are different. The inverse susceptibilities are not linear at temperatures lower than 300 K, which is strong indication that the Curie-Weiss law is not valid for temperatures lower than 300 K. From the detail of susceptibility measurement along $c-$axis (fig. 2.15) we can see the shifting of ordering temperature to the lower temperatures with applied field.

$GdFe_2Si_2$

The Gd^{3+} ion is in the $s-$state and hence no anisotropy caused by crystal field is expected. On the other hand, when we compare magnetization measurements along the $a-$axis (fig. 2.16) and along the $c-$axis (fig. 2.17), one can see that for the $c-$axis, there is small hysteresis even above the ordering temperature. The magnetic moment saturates in both cases at field $B = 4$ T to the value $\mu = 7\mu_B$/f.u. (the effective moment of Gd^{3+} is 8 μ_B).

The temperature dependence of the inverse susceptibility (fig. 2.18) indicates that the susceptibility obeys the Curie-Weiss law very well. By fitting Curie-Weiss law on the measurements along $a-$axis we estimated effective moment as $\mu_{eff} = 8.24\mu_B$/f.u. and on the measurements along $c-$axis we estimated $\mu_{eff} = 8.26\mu_B$/f.u.

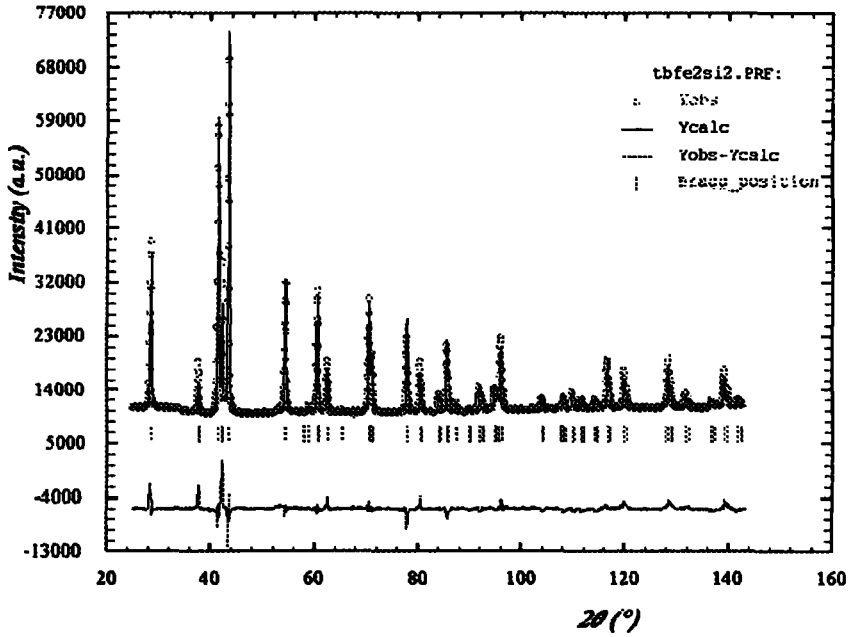

Figure 2.7: Powder diffraction spectra of $TbFe_2Si_2$ and the best fit done using *Fullprof* program.

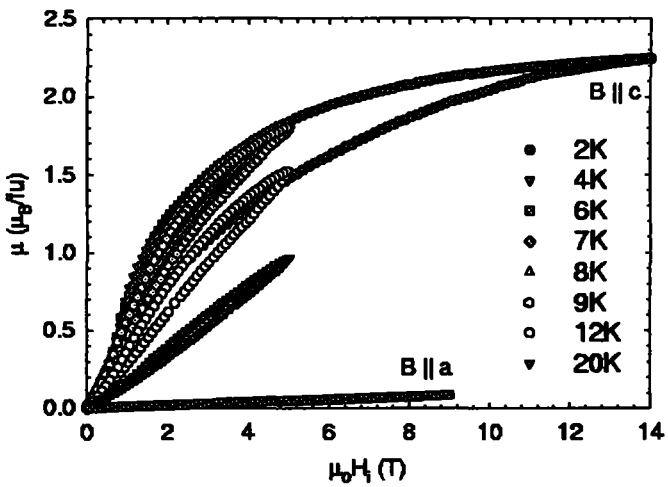

Figure 2.8: Magnetization of $PrFe_2Si_2$ along both principal axes. The a–axis magnetization is linear at all measured temperatures and its temperature dependency is very weak, so only the 2 K curve is shown to simplify the picture.

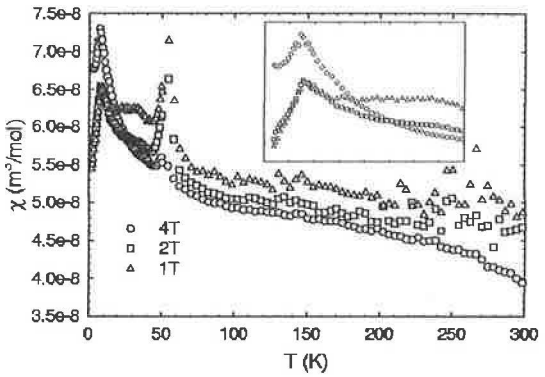

Figure 2.9: The temperature dependence of susceptibility of $PrFe_2Si_2$ measured along $a-$ axis. In insert the low temperature detail is shown.

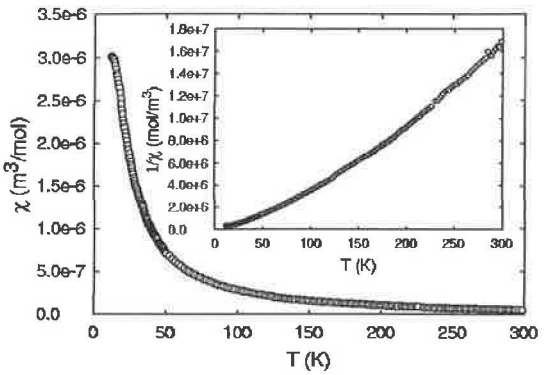

Figure 2.10: The temperature dependence of susceptibility and inverse susceptibility of $PrFe_2Si_2$ measured along $c-$ axis.

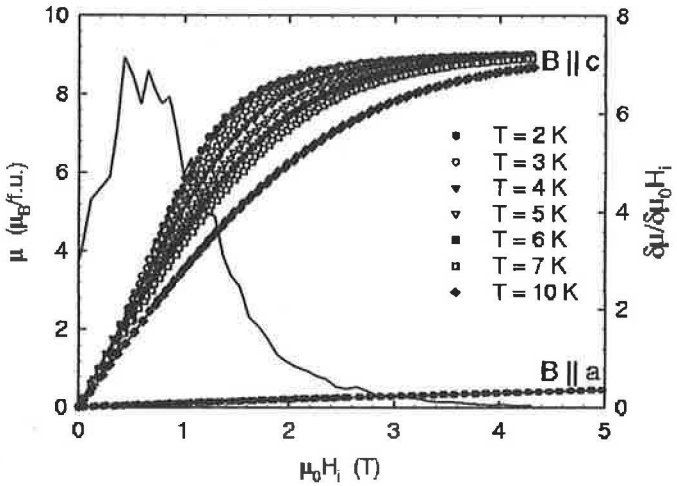

Figure 2.11: Magnetization of $TbFe_2Si_2$ along both principal axes. As the magnetization along the $a-$axis doesn't depend on temperature, only the 2 K curve is shown to simplify the picture. The line represents the derivation of magnetization at temperature 2 K.

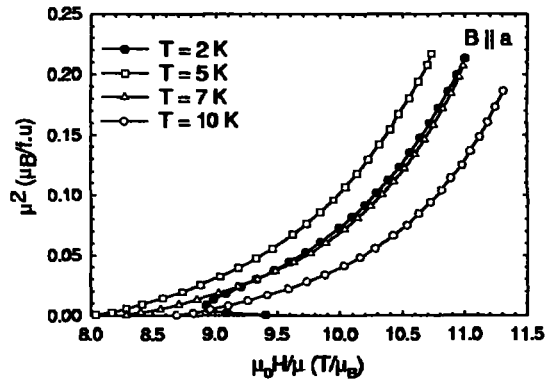

Figure 2.12: Arrot plots of magnetization vs. field along the a−axis for $TbFe_2Si_2$ compound. The magnetization curves exhibit a small hysteresis, so only data for decreasing field are displayed.

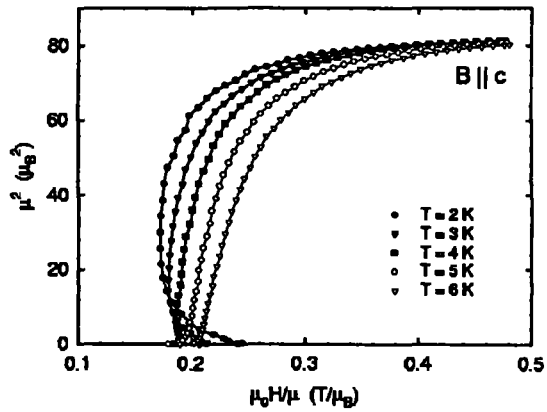

Figure 2.13: Arrot plots of magnetization vs. field for $TbFe_2Si_2$ with applied field along c−axis.

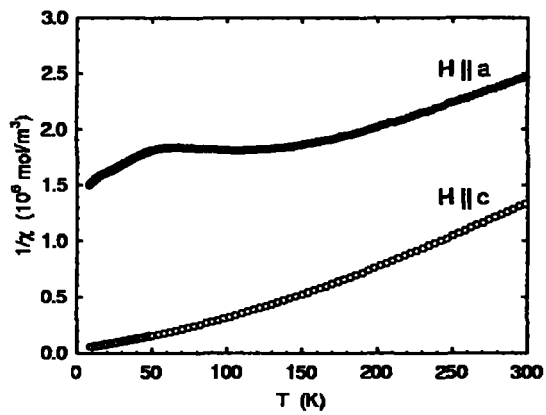

Figure 2.14: The comparison of $TbFe_2Si_2$ inverse susceptibilities measured along both principal axes.

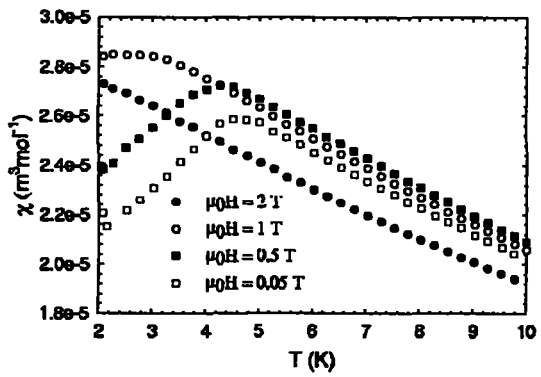

Figure 2.15: The detail of $TbFe_2Si_2$ susceptibility measured along c−axis.

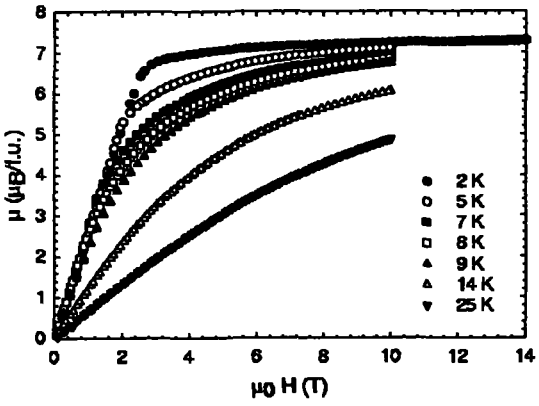

Figure 2.16: Magnetization vs. applied magnetic field in $GdFe_2Si_2$ measured along $a-$ axis.

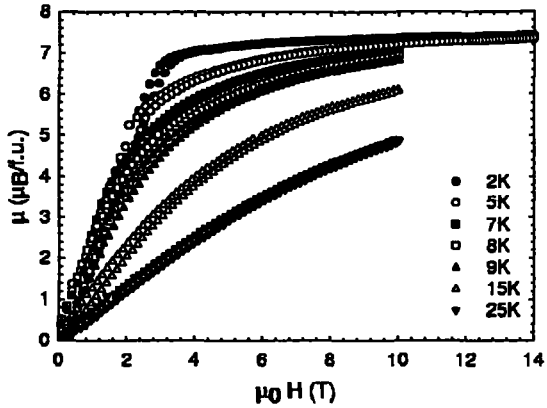

Figure 2.17: Magnetization vs. applied magnetic field in $GdFe_2Si_2$ measured along $c-$ axis. We can see hysteresis even at temperatures above the ordering temperature.

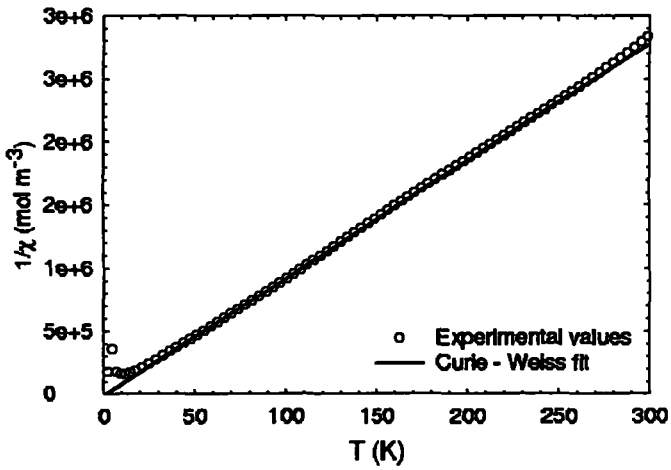

Figure 2.18: The temperature dependence of inverse susceptibility of $GdFe_2Si_2$ measured along $c-$axis. Because temperature dependence along $a-$axis is very similar, we present only result along $c-$axis.

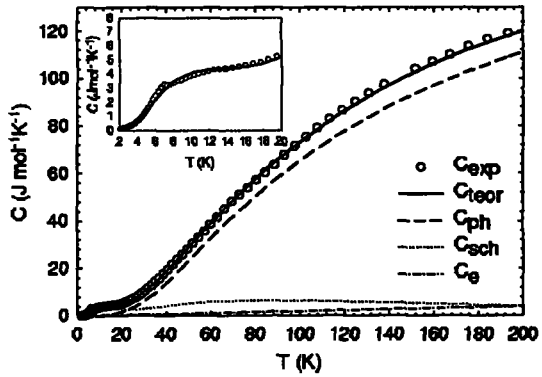

Figure 2.19: The temperature dependence of specific heat of $PrFe_2Si_2$ measured without field. In insert the low temperature detail is presented.

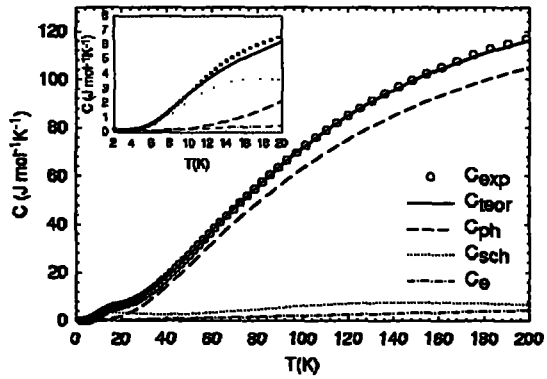

Figure 2.20: The temperature dependence of specific heat of $PrFe_2Si_2$ measured in field $\mu_0 H = 5T$. In insert the low temperature detail is presented.

Type of branch	Degeneracy	Characteristic temperature Θ_N (K)	Anharmonicity coefficient α_N ($10^{-4}K^{-1}$)
D	3	204	2
E_1	4	490	1
E_2	2	490	2
E_3	6	240	4

Table 2.3: Phonon contribution to specific heat of $PrFe_2Si_2$ compound.

2.3.3 Specific heat.

$PrFe_2Si_2$

On temperature dependence of specific heat of $PrFe_2Si_2$ measured in zero field (see fig. 2.19) we can see small peak at temperature $T = 7$ K. This peak is associated with magnetic phase transition from the paramagnetic to the ordered state. At these temperatures, there is also broad bump, which we associate with Schottky contribution to specific heat. When we compare specific heat measurements in zero field and in field $\mu_0 H = 5T$ (fig. 2.19 and 2.20 respectively), this bump is shifted in field to the higher temperatures. The best fit of phonon contribution to specific heat is summarized in table 2.3.

When we subtract phonon and electron contribution from the specific heat, we can obtain the magnetic contribution to the specific heat. Comparison of the magnetic contributions in the zero and elevated magnetic field are plotted in figure 2.21. As we can see, magnetic field broadened the level splitting and shifted Schottky contribution to the higher temperatures. Pr^{3+} ion have $J = 4$ and tetragonal crystal field splits ground state multiplet to 2 doublets and 5 singlets and the magnetic field

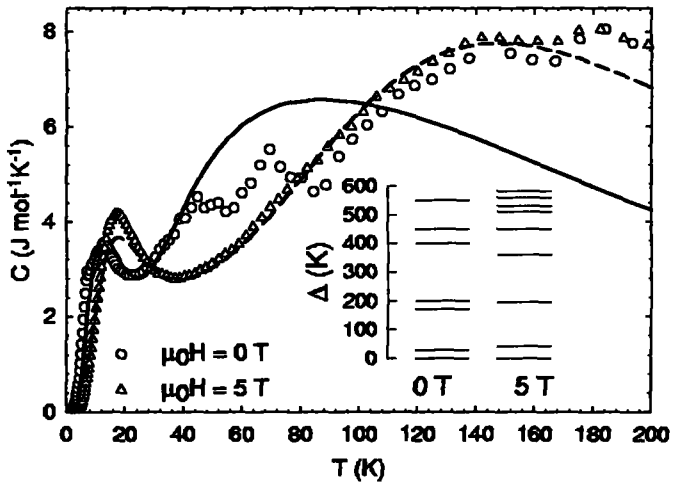

Figure 2.21: The comparison of magnetic and Schottky contribution of $PrFe_2Si_2$ to specific heat at zero field and in field $\mu_0 H = 5$ T. The lines represents the best fit of experimental values. In insert the splitting of ground state level caused by crystal field is plotted.

lifts the degeneracy of the doublets. The best fits obtained for measurements in zero field and in field $\mu_0 H = 5T$ are summarized in table 2.4.

$TbFe_2Si_2$

In zero field, the temperature dependence of specific heat (fig. 2.22) shows a maximum at temperature $T = 5$ K and at high temperatures saturates according to Dulong-Petit law. The peak at $T = 5$ K is associated with transition from paramagnetic to the ordered state. The characteristic temperatures of the best fit of phonon contribution to the specific heat are summarized in table 2.5.

By applying magnetic field to $TbFe_2Si_2$ (2.23) the peak at $T = 5$ K (from magnetic phase transition) shifts to the higher temperatures and almost merges with Schottky contribution to specific heat (fig. 2.24). The crystal field splits ground state to 3 doublets and 7 singlets, the applied external field can lift the degeneracy of the doublets. The comparison of crystal field splitting is summarized in table 2.6 and plotted as insert in figure 2.24.

$GdFe_2Si_2$

In the figures 2.25 and 2.26 we can see a comparison of the temperature dependence of the specific heat of $GdFe_2Si_2$ compound. We can see a lambda-shaped peak with maximum at the temperature $T = 8$ K in zero field data (which can be associated with the magnetic phase transition). At high temperatures the specific heat saturates according to the Dulong-Petit law similar as in the other compounds. The best fit results of phonon spectra are summarized in table 2.7.

i	Δ_i (K); applied field $\mu_0 H = 0$ T	Δ_i (K); applied field $\mu_0 H = 5$ T
0	0	0
1	30	42
2	171	195
3	171	360
4	200	450
5	400	510
6	450	530
7	450	560
8	550	580

Table 2.4: Comparison of crystal field splitting Δ_i in zero field and in field $\mu_0 H = 5$ T obtained from specific heat measurements on $PrFe_2Si_2$ compound.

Type of branch	Degeneracy	Characteristic temperature Θ_N (K)	Anharmonicity coefficient α_N ($10^{-4}K^{-1}$)
D	3	183	2
E_1	6	234	5
E_2	2	385	7
E_3	4	515	9

Table 2.5: Phonon contribution to the specific heat of the $TbFe_2Si_2$ compound.

Gd is supposed to be in the s−state, so no splitting cased by crystal field is expected. The only magnetic contribution to the specific heat is due to the magnetic phase transition at $T = 8$ K. By comparing magnetic contribution to the specific heat in zero field and in field $\mu_0 H = 5$ T (fig. 2.27) we can see that the lambda peak, which is characteristic for transition of the first order changed to some dull maximum, which is characteristic for the second order-type transition. From this, we can conclude that the metamagnetic transition to ferromagnetic ordered state occurs in field lower than 5 T.

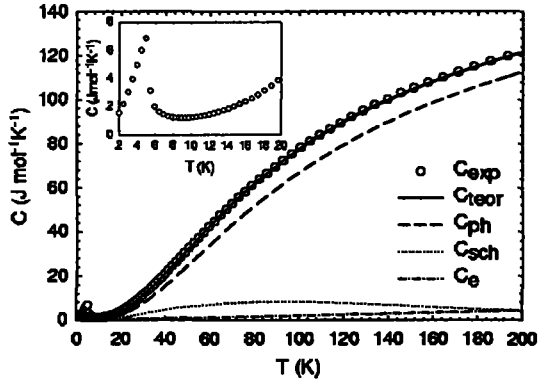

Figure 2.22: The temperature dependence of specific heat of $TbFe_2Si_2$ compound measured in zero field.

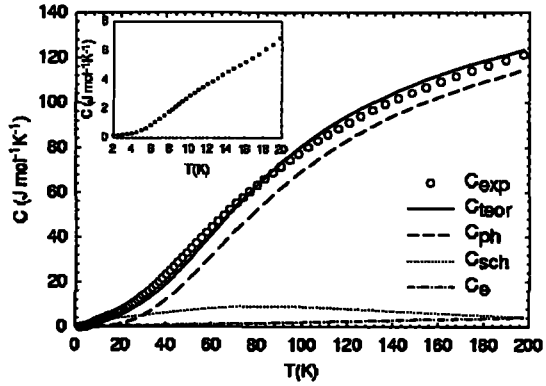

Figure 2.23: The temperature dependence of specific heat of $TbFe_2Si_2$ compound measured in field $\mu_0 H = 5$ T.

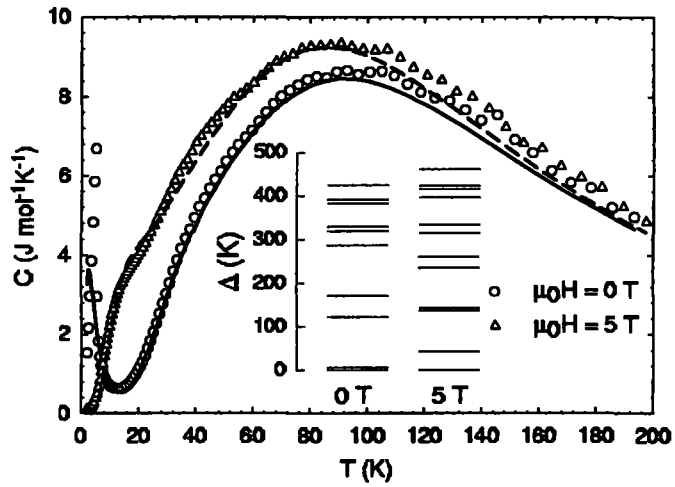

Figure 2.24: The comparison of magnetic and Schottky contribution of $TbFe_2Si_2$ to specific heat in zero field and in field $\mu_0 H = 5$ T. The lines represents the best fit of experimental values. In insert the calculated splitting of ground state level caused by crystal field is shown.

i	Δ_i (K); applied field $\mu_0 H = 0$ T	Δ_i (K); applied field $\mu_0 H = 5$ T
0	0	0
1	6.3	43
2	122	137
3	122	142
4	171	235
5	287	260
6	319	315
7	329	333
8	383	397
9	383	416
10	390	424
11	425	445
12	425	461

Table 2.6: Comparison of crystal field splitting Δ_i in zero field and in field $\mu_0 H = 5$ T obtained from specific heat measurements on $TbFe_2Si_2$ compound.

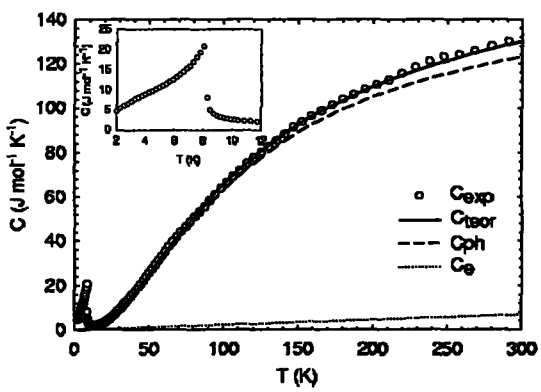

Figure 2.25: The temperature dependence of specific heat of $GdFe_2Si_2$ measured in zero field.

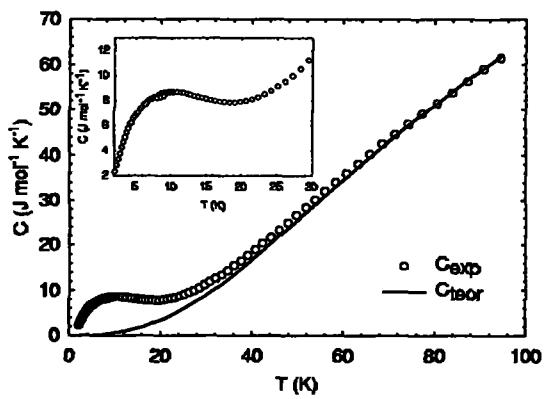

Figure 2.26: The temperature dependence of specific heat of $GdFe_2Si_2$ measured in field $\mu_0 H = 5$ T.

Type of branch	Degeneracy	Characteristic temperature Θ_N (K)	Anharmonicity coefficient α_N ($10^{-4}K^{-1}$)
D	3	170	3
E_1	6	245	3
E_2	4	482	3
E_3	2	520	4

Table 2.7: Phonon contribution to specific heat of $GdFe_2Si_2$ compound.

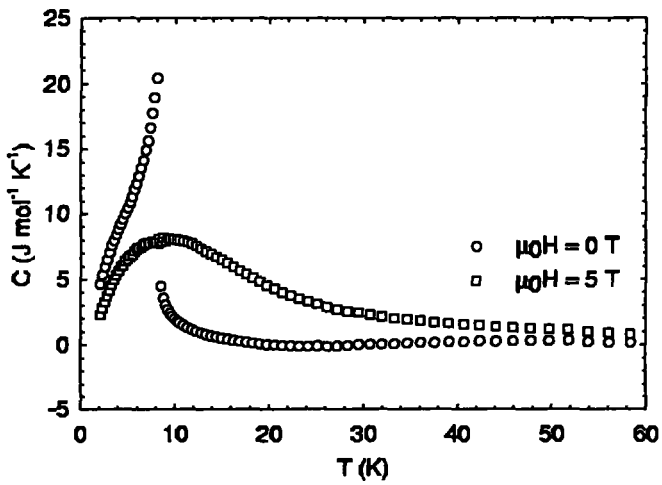

Figure 2.27: The temperature dependence of contributions to specific heat of $GdFe_2Si_2$ due to magnetic phase transition.

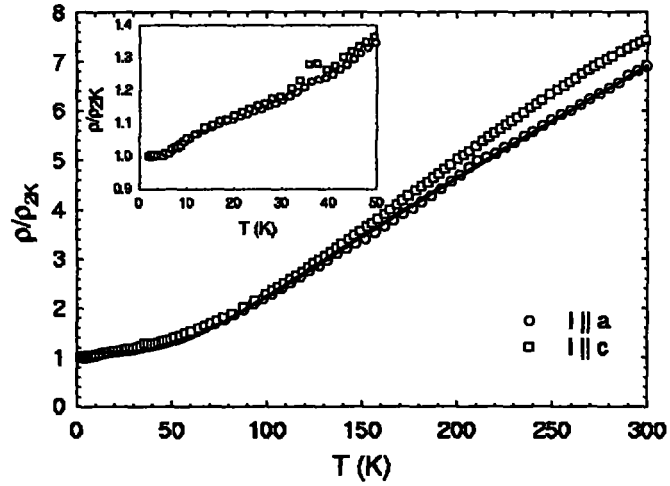

Figure 2.28: The temperature dependencies of resistivity of $PrFe_2Si_2$ measured along $a-$ and $c-$axis. The full fine represents the best fit of experimental data.

2.3.4 Electrical resistivity.

$PrFe_2Si_2$

There is no indication of magnetic phase transition to ordered state on temperature dependence of resistivity (fig. 2.28) measured along both principal axes. Instead of this, there is a broad bump with maximum at about 14 K, which can be suppressed by the applied magnetic field (the discussion of this effect is in section 2.3.5). The peak at 37 K is an apparatus effect. In the paramagnetic state the resistivity decreases almost linearly with decreasing temperature. We tried to fit Bloch-Grüneissen law (equation 1.49) to the resistivity data. For the $a-$axis data we obtained characteristic temperature $\Theta = 345$ K and temperature independent constant $C = 0.34$. The discrepancy between the fit and the experimental data is because of a broad bump, probably of magnetic origin. The dependence measured along $c-$axis doesn't obey Bloch-Grüneissen law at all.

To check the quality of the crystal we determined *RRR*. The *RRR* for $a-$axis is 6.94 and for $c-$axis 7.46. The difference between *RRR*s along both crystallographic axes may be caused by inhomogeneities in sample, like micro-cracks or other defects.

$TbFe_2Si_2$

The temperature dependencies of resistivity of $TbFe_2Si_2$ (fig. 2.29) measured along both principal axes show local minima at temperature $T = 10$ K. Below 10 K the resistivity increases with decreasing temperature, which can be ascribed to the onset of the antiferromagnetic short-range ordering. This increase terminates around 4 K, which is below the ordering temperature. In case of $a-$axis the resistivity

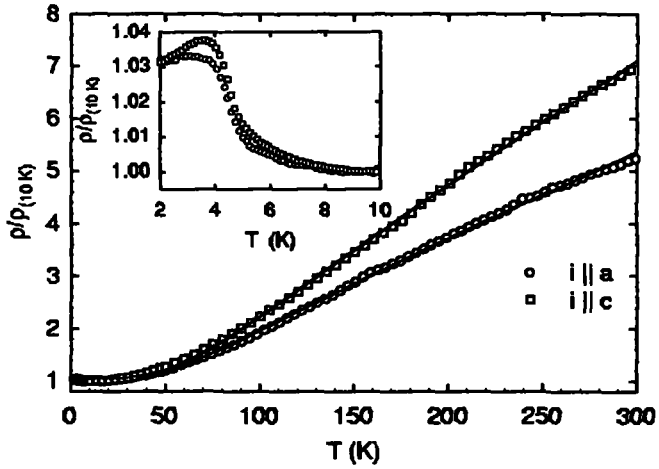

Figure 2.29: The temperature dependencies of resistivity of $TbFe_2Si_2$ compound. The resistivity data are related to the resistivity at 10 K to better visualize the anisotropy of the resistivity. The resistivity at temperature 10 K measured along $a-$axis is $R_{10a} = 28.1$ $\mu\Omega$cm and along $c-$axis $R_{10c} = 69.2$ $\mu\Omega$cm. The lines represents the best fit.

below 4 K is temperature independent, while along $c-$axis, the resistivity decreases with decreasing temperature. In the temperature region 10 – 300 K both dependencies obey the Bloch-Grüneissen law (equation 1.49). For $a-$axis we obtained: $C = 0.43$ and $\Theta = 309$ K. For $c-$axis we obtained: $C = 1.50$ and $\Theta = 352$ K.

To check the quality of the crystal we determined *RRR*. The *RRR* for $a-$ and $c-$axis is 5.1 and 6.8, respectively. The difference between *RRR*s along both crystallographic axes may be caused by inhomogeneities in sample, like micro-cracks or other defects.

$GdFe_2Si_2$

On the temperature dependencies of resistivity of $GdFe_2Si_2$ measured along both axes the transition from paramagnetic to ordered state at 8 K is clearly visible (fig. 2.30). The transition temperature obtained from the resistivity is in very good agreement with the transition temperature obtained from the specific heat. Under this temperature the resistivity decreases in both cases linearly with decreasing temperature. Above the temperature $T = 8$ K the resistivity obeys Bloch-Grüniessen law (equation 1.49). From the fit of the temperature dependence measured along $a-$ and $c-$axis we determined $C = 0.35$, $\Theta = 368$ K and $C = 0.39$, $\Theta = 281$ K respectively.

To check the quality of the crystal we determined *RRR*. The *RRR* for $a-$ and $c-$axis is 7.32 and 5.85 respectively. The studied compound form layered structure with easy-cleaving plane perpendicular to $c-$axis and different *RRR* along both axes may be caused by micro-cracks in this structure.

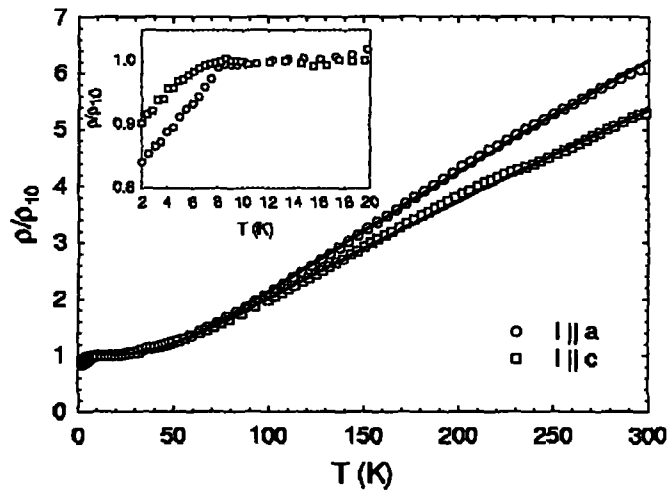

Figure 2.30: The temperature dependencies of resistivity of $GdFe_2Si_2$ measured along both principal axes. The lines represents the best theoretical fit.

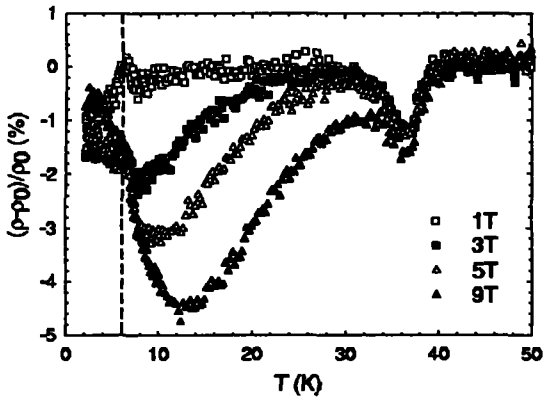

Figure 2.31: The temperature dependences of magnetoresistivity of $PrFe_2Si_2$ compound. The electric current was applied along the a–axis and the magnetic field was applied along the c–axis. The dashed line represents the ordering temperature obtained from the specific heat measurements.

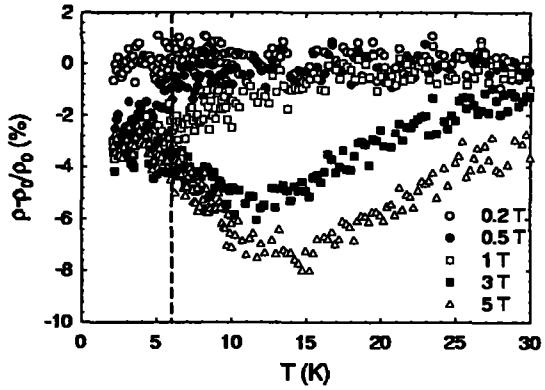

Figure 2.32: The temperature dependences of transversal magnetoresistivity of $PrFe_2Si_2$ compound. The electric current was applied along the c–axis. The dashed line represents the ordering temperature obtained from the specific heat measurements.

2.3.5 Magnetoresistivity.

$PrFe_2Si_2$

At low temperatures, there is bump on the temperature dependence of the electrical resistivity of $PrFe_2Si_2$ measured along a–axis. This bump can be suppressed by the applied magnetic field along c–axis. To emphasize this effect we decided to plot $(\rho_B - \rho_0)/\rho_0$ plot (fig. 2.31). The other effect, which can be seen from this figure is a peak at the ordering temperature in the applied field $B = 1$ T. This peak is characteristic for paramagnetic↔antiferromagnetic transition (compare with the theoretical figure 1.6). At higher fields, this peak disappears, which indicates, that the character of the transition has changed. The minimum at the temperature $T = 36$ K is an apparatus effect and has no physical relation to studied properties.

At the temperature dependence of the transversal magnetoresistivity measured with electric current applied parallel to c–axis (fig. 2.32) we found the elimination of the bump just above the transition temperature.

At the temperature dependence of longitudinal magnetoresistivity in both cases we found no anomaly at the transition temperature and no dependency on the magnetic field.

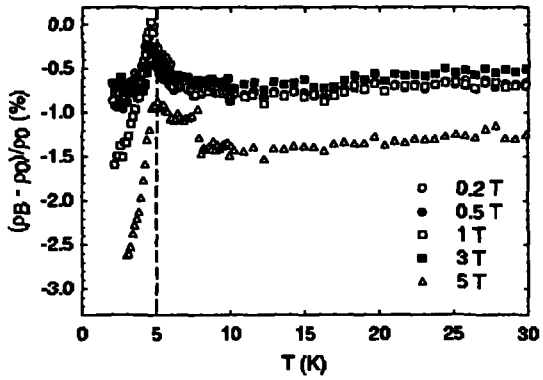

Figure 2.33: The temperature dependences of longitudinal magnetoresistivity of $TbFe_2Si_2$ compound. The electric current was applied along $a-$axis. The dashed line represents the ordering temperature obtained from the specific heat measurements.

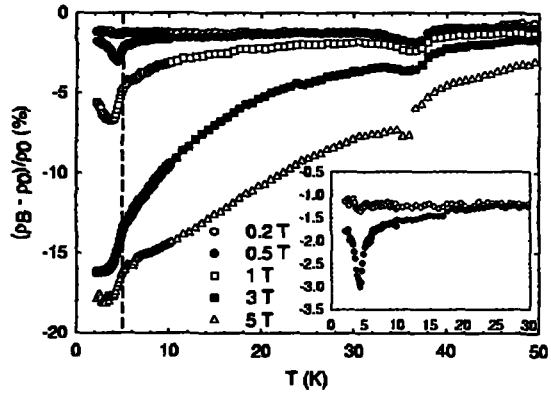

Figure 2.34: The temperature dependences of transversal magnetoresistivity of $TbFe_2Si_2$ compound. The electric current was applied along $a-$axis and the magnetic field was applied along $c-$axis. In the insert, the low field dependences are emphasized. The dashed line represents the ordering temperature obtained from the specific heat measurement.

$TbFe_2Si_2$

In case of $TbFe_2Si_2$ we measured magnetoresistivity along both principal axes and in both geometrical orientations. In all cases the anomaly associated with the magnetic phase transition is situated slightly below the ordering temperature obtained from the specific heat measurements. In case of $a-$axis and magnetic field applied parallel to the electric current (fig. 2.33), we can see sharp lambda-shaped maximum below ordering temperature. Below this maximum, magnetoresistivity rapidly decreases. On the other hand, in case of current applied along $a-$axis and magnetic field applied along $c-$axis (fig. 2.34) we observed minimum below the transition temperature. This effect in field $B = 5$ T reaches about 18.5 %. The effect shows that magnetic field less than 0.5 T is sufficient to the field-induced ferromagnetic order.

In case of the longitudinal magnetoresistivity along the $c-$axis (fig. 2.35) we observed temperature dependence, which is typical for paramagnetic↔antiferromagnetic transition in fields up to $B = 1$ T. In higher fields the shape changes to the typical paramagnetic↔ferromagnetic dependence. From this result we can conclude, that the field-induced antiferromagnetic↔ferromagnetic phase transition occurs in field between 1 T and 3 T. In the case of the electric current applied along the $c-$axis and the magnetic field applied along the $a-$axis (fig. 2.36) we observed only local minimum at temperature slightly below the ordering temperature. The local minimum at temperature $T = 38$ K is again an apparatus effect and has no relation with studied effects.

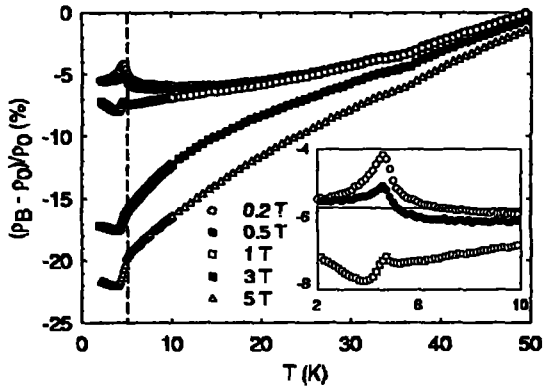

Figure 2.35: The temperature and field dependence of parallel magnetoresistivity of $TbFe_2Si_2$ compound with electric current applied along the c–axis. In insert the paramagnetic↔antiferromagnetic transition is emphasized. The dashed line represents the ordering temperature obtained from the specific heat measurements.

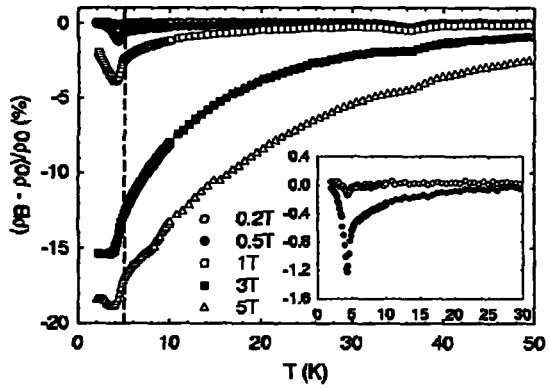

Figure 2.36: The temperature and field dependence of transversal magnetoresistivity of $TbFe_2Si_2$ compound. The electric current was applied along c–axis. The dashed line represents the ordering temperature obtained from the specific heat measurements.

$GdFe_2Si_2$

The parallel (fig 2.37) and perpendicular (fig. 2.38) temperature dependences of magnetoresistivity measured along the a–axis of $GdFe_2Si_2$ are very similar. This may be caused by the fact, that Gd^{3+} free ion is in the s–state. In both cases there is local minimum at the ordering temperature, which is deeper with higher applied field. The shape of the minima indicates the field-induced paramagnetic↔ferromagnetic phase transition in all applied fields.

The parallel (fig 2.39) and perpendicular (fig. 2.40) temperature dependencies of magnetoresistivity measured along c–axis are very similar too. There the minimum at the transition temperature is observable only on the 1 T data. In higher fields, the relative magnetoresistivity tend to decrease even at the lowest reachable temperatures. The minimum at 36 K is again the apparatus effect on the dependence measured in zero field.

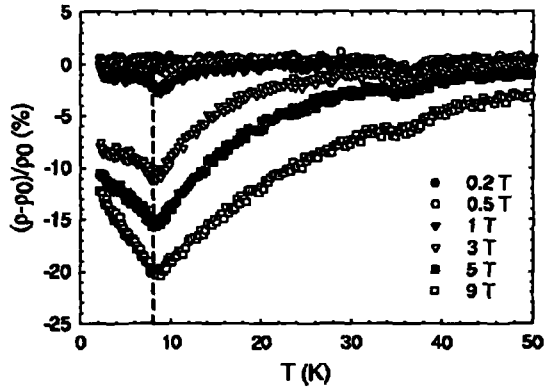

Figure 2.37: The relative longitudinal magnetoresistivity measured in $GdFe_2Si_2$ with electric current applied along the a−axis. The dashed line represents ordering temperature obtained from specific heat measurements.

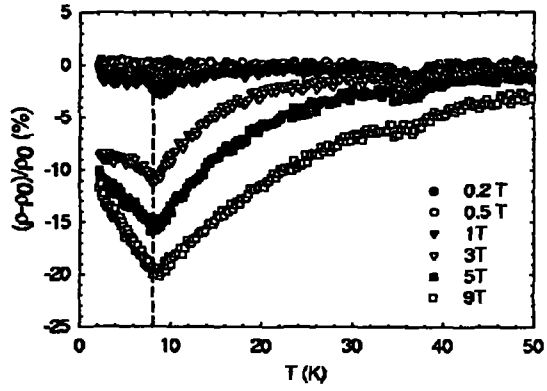

Figure 2.38: The relative magnetoresistivity measured in $GdFe_2Si_2$ with electric current applied along a−axis and magnetic field applied along c−axis. The dashed line represents the ordering temperature obtained from the specific heat measurements.

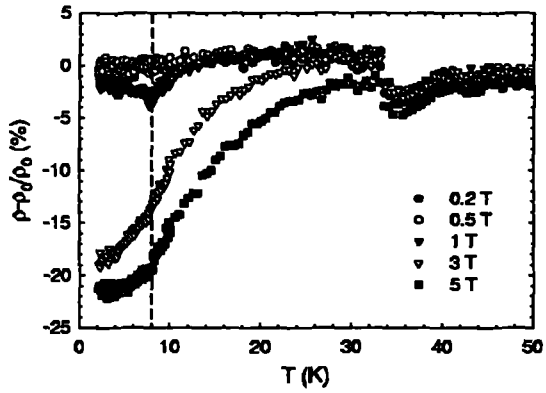

Figure 2.39: The relative parallel magnetoresistivity measured in $GdFe_2Si_2$ with electric current applied along the c−axis. The dashed line represents ordering temperature obtained from the specific heat measurements.

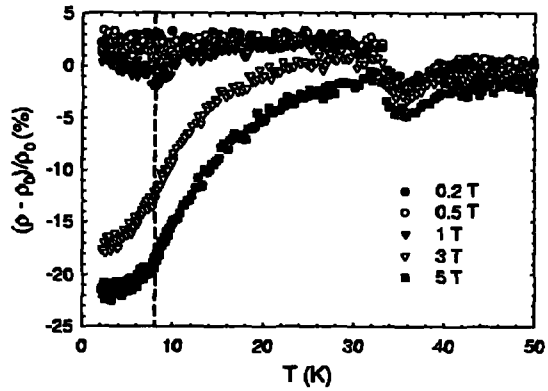

Figure 2.40: The relative magnetoresistivity measured in $GdFe_2Si_2$ with electric current applied along the c−axis and magnetic field applied along the a−axis.The dashed line represents ordering temperature obtained from the specific heat measurements.

Chapter 3

Conclusions

In this diploma work, magnetic properties, heat capacity and electrical resistivity of selected $REFe_2Si_2$ rare–earth intermetallic compounds have been extensively studied on the single crystals. Possession of the single crystals enable us to pay attention to study manifestations of the crystal anisotropy in measured physical quantities. The main results can be summarized as follows:

Good quality single crystals of $REFe_2Si_2$ compounds (RE = Pr, Tb, Gd, Dy) have been grown by the Czochralski method in a "tri-arc" furnace. The crystals have strong tendency to cleave in the basal plane. No second phase has been detected by X-ray powder diffraction, but the presence of small amounts of ferromagnetic impurities has been found by magnetization measurements on all compounds.

All studied compounds order antiferromagnetically at low temperatures. Anomalies in temperature dependences of magnetization, heat capacity and electrical resistivity indicate transition temperatures T_N = 7.2 K, 5.2 K and 8 K for $PrFe_2Si_2$, $TbFe_2Si_2$ and $GdFe_2Si_2$, respectively. All compounds have tendency to undergo a field induced metamagnetic transition.

Magnetization and susceptibility measurements on $PrFe_2Si_2$ and $TbFe_2Si_2$ compounds revealed strong uniaxial anisotropy as well in magnetic ordered state as in paramagnetic state. In both cases the $c-$axis is an easy axis of magnetization. For $PrFe_2Si_2$ the magnetic moment measured along $a-$axis depends linearly on the applied magnetic field up to $B = 9$ T and measurements along $c-$axis show the saturated magnetic moment $\mu = 2.25\mu_B$/f.u. at $B = 14$ T. In the case of $TbFe_2Si_2$ the magnetization along the $c-$axis saturates towards the value $\mu = 9\mu_B$/f.u. and in the case of $a-$axis, the magnetization is almost linear, not exceeding $\mu = 0.5\mu_B$/f.u. The Curie–Weiss law can not be used for describing temperature dependency of susceptibility in the both compounds in temperatures below 300 K.

In accordance with our expectation, magnetization measurements did not reveal strong anisotropy in the case of $GdFe_2Si_2$ single crystal. The susceptibility data follow the Curie–Weiss law yielding the effective moment $\mu_{eff} = 8.24\mu_B$. From the magnetization measurements at $T = 2$ K we found that the magnetic moment saturates in field about 4 T to the value $\mu = 7\mu_B$/f.u.

Using comparative analysis of specific heat we were able to find for all samples the complete set of

parameters describing the phonon, magnetic and optionally Schottky contribution to the specific heat. The ground-level splitting caused by the crystal electric field (CEF) for $PrFe_2Si_2$ and $TbFe_2Si_2$ at zero field and in field $B = 5$ T was derived for these compounds. The ground state of $GdFe_2Si_2$ is symmetric, so no CEF splitting was supposed.

An anisotropy has been found in temperature dependence of resistivity on all samples. The resistivity measurements revealed small deviations from Bloch-Grüneissen law above the ordering temperature in all cases. The anomaly associated with the ordering temperature is clearly visible in $TbFe_2Si_2$ and $GdFe_2Si_2$.

Magnetoresistivity measurements have detected metamagnetic transition in $TbFe_2Si_2$ measured with electric current applied along the $c-$axis and in magnetic field applied parallel to the electric current. In all other cases we observed only field-induced-like ferromagnetic state dependence.

In conclusion we can summarize that the anisotropic behavior of magnetization, susceptibility, electrical resistivity and magnetoresistivity of $REFe_2Si_2$ compounds for RE = Pr, Tb, Gd has been studied on good quality single crystals. In close future we would like to extend our study to $DyFe_2Si_2$ single crystal and later to the other $REFe_2Si_2$ compounds with heavy rare-earth ion.

Bibliography

[1] N. W. Ashkroft and N. D. Mermin, Solid State Physics (Saunders College Publishyng 1976), 30.

[2] R. G. Lerner and G. L. Trigg, Encyclopedia of Physics, VCH Publishers New York (1991).

[3] Ch. Kittel, Úvod do fyziky pevných látek, Academia Praha, 1985.

[4] Karel Prokeš, Magnetism in uranium intermetallic compounds, Van der Waals-Zeeman Institut Amsterdam, 1997.

[5] P. Svoboda, P. Javorský, M. Diviš, V. Sechovský, F. Honda, G. Oomi and A. A. Menovsky, Phys. Rew. B **63** (2001), 212408.

[6] The Encyklopedia of Materials, Elsevier Science Publishers, 2001.

[7] M. Rotter, M. Doerr, M. Loewenhaupt, U. Whitte, P. Svoboda, J. Vejpravová, H. Sassik, C. Ritter, D. Eckert, A. Handstein and D. Hinz, Phys. Rew. B **64** (2001), 134405.

[8] E. Gratz and H. Nowotny, Physica B **130** (1985), 75.

[9] N.H. Andersen and H. Smith, Phys. Rew B **19** (1979), 384.

[10] H. Yamada and S. Takada J. Phys. Soc. Jpn. **34** (1973), 51.

[11] C. M. Hurd, The Hall Effect in Metals and Alloys, Plenum New York, 1972.

[12] Y. Kawasaki, K. Ishida, T. Mito, C. Thessieu, G.-q. Zheng, Y. Kitaoka, C. Geibel and F. Steglich, Phys. Rew. B **63** (2001), 140501.

[13] A. Krimmel, J. Hemberger, M. Nicklas, G. Knebel, W. Trinkl, M. Brando, V. Fritsch, A. Loidl and E. Ressouche, Phys. Rew. B **59** (1999), 6604.

[14] M.N. Groshev, M. D. Koterlin, E. M. Levin, R. V. Lutsiv, N. M. Miftakhov, Yu. P. Smirnov, A. E. Sovestnov, A. V. Tyunis, V. A. Shaburov, R. I. Yasmitskil, S. M. Kuzmina, V. I. Yetrova and V. A. Tyukavin, Sov. Phys. Solid State **28–29** (1986), 1519.

[15] G. Liang, M. Croft, R. Neifeld and B. Qi, J. Appl. Phys. **61** (1987), 3183.

[16] E. V. Sampathkumaran, R. Vijayaraghavan, P. Sen and C. N. R. Rao, Solid State Commun. **63** (1987), 34.

[17] J. A. Blanco, D. Schmitt and J. C. Gomez-Sal, J. Magn. Magn. Mater. **116** (1992), 128.

[18] D. Gignoux and D. Schmitt, in the Handbook on the Physics and chemistry of Rare Earths, Vol. **20** (1993).

[19] F. Lapierre, P. Haen, R. Briggs, A. Hamzić, A. Fert and J. P. Kappler, J. Magn. Magn. Mater **63–64** (1987), 338.

[20] P. Svoboda, J. Vejpravová, F. Honda, E. Šantavá, O. Schneeweiss and T. Komatsubara, Physica B **328** (2003), 139.

[21] V. Ivanov and A. Szytula, J. of Alloys and Compounds **262 – 263** (1997), 253.

[22] A. V. Morozkin, Yu. D. Seropegin, A. V. Gribanov and J. M. Barakatova, J. of Alloys and Compounds **256** (1997), 175.

[23] A. Blaise, B. Fak, J. P. Sanchez, G. Amoretti, P. Santini, R. Caciuffo, D. Schmitt, B. Malaman and G. Venturini, J. of Physics: Condensed matter **7** (1995), 8317.

[24] I. Felner, I. Mayer A. Grill and M. Schieber, Solid State Commun. **16** (1975), 1005.

[25] G. Czjzek, V. Oestreich, H. Schmidt, K. Latka and K. Tomala, J. Magn. and Magn. Mater. **79** (1989), 42.

[26] H. M. Duh, I. S. Lyubutin, Y. C. Chen, H. F. Chen and C. H Lin, J. of Physics: Condensed matter **10** (1998), 4457.

[27] D. R. Noakes, A. M. Umarji and G. K. Shenoy, J. Magn. and Magn. Mater. **39** (1983), 309.

[28] B. Malaman, G. Venturini, A. Blaise, G. Amoretti and J. P. Sanchez, J. Magn. Magn. Mater. **104 – 107** (1992), 1359.

[29] B. Malaman, G. Venturini, A. Blaise, J. P. Sanchez and G. Amoretti, Phys. Rew. B **47** (1993), 8681.

[30] J. Vejpravová, P. Svoboda, V. Sechovský, M. Janeček and T. Komatsubara, Physica B **328** (2003), 173.

[31] E. R. Bauminger, I. Felner, D. Froindlich, A. Grill, D. Lebenbaum, I. Mayer, I. Novik, S. Ofer and M. Schieber, Proc. Int. Conf. Magetism, Moscow, August 1973.

[32] H. Pinto, M. Melamud, M. Kuznietz and H. Shaked, Phys. Rev B **31** (1985), 508.

[33] A. A. Menovsky and J. J. M. Franse, J. Cryst. Growth **65** (1983), 286.

[34] V. Valvoda, M. Polcarová and P. Lukáč, Základy strukturní analýzy, Karolinum Praha, (1992).

[35] http://www.ccp14.ac.uk/tutorial/lmgp/orientexpress.htm

[36] http://www-llb.cea.fr/fullweb/fp2k/fp2k.htm

[37] http://www-llb.cea.fr/winplotr/winplotr.htm

[38] J. Baruchel, J. L. Hodeau, M. S. Lehmann, J. R. Regrand, C. Schlenker, Neutron and synchrotron radiation for condensed matter studies, Springer-Verlag, 1993.

[39] J. Brož a kolektív, Základy fysikálních měření, Státní Pedagogické nakladatelství Praha, 1967.

[40] http://www.qdusa.com/products/ppms.html

[41] J. S. Hwang, K. J. Lin and Ch. Tien, Rev. Sci. Instrum. **68** (1997), 94.